SAND2006-4522

# Optimization of Strain-Relaxed $InP_yAs1$-y Buffers for InGaAs Thermophotovoltaic Devices

**By Jeffrey G. Cederberg and Stephen R. Lee**

**Table of Contents**

List of Figures ..... 3
List of Tables ..... 5
1 Scope of research ..... 6
1.1 Introduction ..... 6
1.1.1 *Ex situ* Characterization of Strain and Composition ..... 7
1.1.2 Microscopic Characterization of Threading Dislocation Density ..... 8
1.1.3 Chemical threading dislocation identification. ..... 9
1.2 Summary ..... 10
2 *Ex situ* characterization of strain and composition using high resolution x-ray diffraction reciprocal space mapping. ..... 11
2.1 Introduction ..... 11
2.2 Preliminary evaluation of available reflections ..... 12
2.3 Strain and composition determination using HRXRD/RSM ..... 16
2.3.1 Single InPAs layers on InP ..... 16
2.3.2 Equilibrium models of layer relaxation ..... 18
2.3.3 Transverse linewidth analysis of single InPAs heterostructures ..... 19
2.4 InPAs buffers ..... 23
2.4.1 3-step InPAs buffers ..... 23
2.4.2 Linearly graded buffer layers ..... 31
2.4.3 Multi-step graded buffer layers ..... 33
2.5 $In_{0.68}Ga_{0.32}As$ TPV cells on InPAs buffers ..... 35
2.6 Summary ..... 37
3 Etch Chemistries for Evaluation of Threading Dislocation Densities ..... 39
3.1 Introduction ..... 39
3.2 Experimental issues associated with etch pit measurements ..... 39
3.3 Survey of etch chemistries ..... 41
3.4 InPAs dislocation sensitive etch development ..... 43
3.4.1 Experimental details for InPAs etch development ..... 43
3.4.2 H etchant (1:2 HBr:H3PO4) with single InPAs layers ..... 43
3.4.3 H etchant (1:2 HBr:H3PO4) with InPAs buffers ..... 46
3.5 InGaAs dislocation sensitive etch development ..... 47
3.5.1 Experimental details for InGaAs etch development ..... 47
3.5.2 H etchant (1:2 HBr:H3PO4) with InGaAs ..... 51
3.5.3 AB etchants ($HF:CrO_3:H_2O$) with InGaAs ..... 51
3.5.4 RC-1 ($HF:HNO_3:H_2O$) with InGaAs ..... 54
3.5.5 Illuminated etchants ..... 56
3.6 Summary ..... 61
4 Transmission Electron Microscopy of strain relaxed buffers and TPV devices ..... 63
4.1 Cross-sectional transmission electron microscopy (XTEM) ..... 63
4.2 InGaAs/SiN interfacial analysis. ..... 63
4.3 XTEM analysis of 05-362a and 05-362b. ..... 67
4.4 Plan view TEM sample preparation ..... 69
5 References ..... 72

**List of Figures**

Figure 1 Geometry showing the spatial beam compression for glancing exit geometry. Derivation is included. ..... 15
Figure 2. Residual strain in various single layers either measured in this study or available in the literature. ..... 19
Figure 3. Transverse scans at 0° and 90° azimuths for VE195 ..... 20
Figure 4. Transverse scans at 0° and 90° azimuths for VE196 ..... 21
Figure 5. Microscopy quantifying the linear density of misfit dislocations in VE196 and VE195. a) AFM micrograph of surface showing linear misfit intersection the surface. The density is 1400 $cm^{-1}$, giving a mean spacing of 7 µm. b) TEM micrograph showing the misfit dislocation network. The density is about 6 x $10^4$ $cm^{-1}$, giving a mean spacing of 0.2 µm. ..... 22
Figure 6. Representative RSM for sample 05-360a showing the features measured. a) (004) reflection and b) (335) reflection. ..... 24
Figure 7. Illustration of the diffraction geometry used for x-ray linewidth measurements and the source of the tilt and twist components of the linewidth about $K_x$ and $K_z$, respectively, and the finite size effects associated with the correlation length L. a) Shows the cross-sectional view of the geometry, b) shows the plan view.[14] ..... 28
Figure 8. Transverse peakwidth measurements as a function of interplanar angle with a fit to extract the tilt and twist components of the linewidth. The correlation length cannot be evaluated from the measurements, suggesting the domain size is large. ..... 29
Figure 9. Schematics showing the different regimes where peakwidth techniques might and might not apply. a)III-nitrides on $Al_2O_3$ have a high density of dislocations in the film volume resulted in a reasonable correlation b)The scattering from a thin film with few dislocations is dominated by the misfit dislocation array, and might produce unreasonably high dislocation densities from a peakwidth analysis. c)Scattering from a thick film with many dislocations should produce dislocation densities from the peaklinewidth analysis that agree more favorably. ..... 31
Figure 10. Reciprocal space maps of a linearly graded InPAs buffer (05-366a) with a 1 µm InGaAs layer on top. a) The (004) symmetric reflection and b) the asymmetric (335) reflection. ..... 33
Figure 11. Reciprocal space maps of a step graded InPAs buffer (1-956) top about the a) (004) and b) (444) reflections. ..... 34
Figure 12. RSMs of ve089d, an InGaAs TPV cell on a 3-step InPAs buffer, showing a) the (004) reflection and b) the (335) reflection. ..... 37
Figure 13. The surface of 05-334c undoped $InP_{0.82}As_{0.18}$ after treatment with Huber etchant. Major and minor crystal orientations are at 45° to the axis of the image ..... 44
Figure 14. The surface of 05-331c Te: $InP_{0.82}As_{0.18}$ after treatment with Huber etchant Major and minor crystal orientations are at 45° to the axis of the image. ..... 45
Figure 15. The surface of 05-341c undoped $InP_{0.68}As_{0.32}$ after treatment with Huber etchant Major and minor crystal orientations are at 45° to the axis of the image ..... 46
Figure 16. AFM images showing the a) as-received Zn:InPAs 3-step buffer and b) the etch buffer using the H etchant for 60 sec. ..... 47
Figure 17. AFM images of 4my001-3 a) before chemical treatment and b) after removal of removal of InGaAs contact and InPAs window layers ..... 50

Figure 18. Lamp and experimental equipment used for providing illumination to samples. 51
Figure 19. The surface of 5ey021-3 after chemical treatment to remove the top layers and expose the InGaAs emitter and 60 seconds in the AB etchant. Major and minor crystal orientations are at 45° to the axis of the image. 53
Figure 20. HRXRD about the (004) reflection for the control sample (sample A - red) and samples etched for 60 seconds (sample C – green) and 180 seconds (sample D - blue). No InGaAs cell is left after 180 seconds in the etchant. 53
Figure 21. The surface of 5ey021-3 after chemical treatment to remove the top layers and expose the InGaAs emitter and 30 seconds in the 1:3 AB etchant:HF. Major and minor crystal orientations are at 45° to the axis of the image. 54
Figure 22. AFM image of the control and a 30 second RC-1 etch. The regular cigar shaped pits are replaced by large pyramidal pits. Major and minor crystal orientations are at 45° to the axis of the image. 55
Figure 23. TCXRD taken around (004) showing the control sample (blue curve) and the sample etched for 30 seconds in the RC-1 etchant (red curve). Most of the layers have been removed in a during the etch, leaving only the first buffer layer. 56
Figure 24. The surface of 5ey021-3 after chemical treatment to remove the top layers and expose the InGaAs emitter and 30 seconds in the 1:1 $H_3PO_4$(85%):$H_2O_2$(30%). Major and minor crystal orientations are at 45° to the axis of the image. 57
Figure 25. The surface of 5ey021-3 after chemical treatment to remove the top layers and expose the InGaAs emitter and 30 seconds without illumination in the 1:1:10 HF(48%):$H_2O_2$ (30%):DI $H_2O$ MSO solution. Major and minor crystal orientations are at 45° to the axis of the image. 58
Figure 26. The surface of 5ey021-3 after chemical treatment to remove the top layers and expose the InGaAs emitter and 180 seconds with illumination in the 1:1:10 HF(48%):$H_2O_2$ (30%):DI $H_2O$ MSO etchant. Major and minor crystal orientations are at 45° to the axis of the image. 59
Figure 27. The surface of 5ey021-3 after chemical treatment to remove the top layers and expose the InGaAs emitter and 60 seconds with illumination in the 1:1 HF(48%):$CrO_3$ (33 wt%) Sirtl etchant. Major and minor crystal orientations are at 45° to the axis of the image. 60
Figure 28. The surface of 5ey021-3 after chemical treatment to remove the top layers and expose the InGaAs emitter and 60 seconds with illumination in the 1:1 HF(48%):$CrO_3$ (33 wt%) Sirtl etchant diluted with 4 parts of deionized water. Major and minor crystal orientations are at 45° to the axis of the image. 61
Figure 29. XTEM image of the interface between InGaAs and SiN. Region 1 was used to get information about the interface between these two layers. Region 2 was a control to get the SiN spectrum. Region 3 (not visible in this image) was used to get the InGaAs signal. 65
Figure 30. X-ray spectrum from different areas of NREL 1-1006 Q1. The red spectrum corresponds to the InGaAs layer, the green spectrum from the SiN layer, and the blue spectrum is the interface between the two. 65
Figure 31. X-ray spectrum from the interface layer for NREL 1-1006 Q1 66
Figure 32. X-ray spectrum from the interface layer for NREL 1-1006 Q2 66
Figure 33. X-ray spectrum from the interface layer for NREL 1-1006 Q4 67

Figure 34. XTEM image of 05-362a. The speckled texture is an artifact of the FIB process..... 68
Figure 35. XTEM image of 05-362b. The speckled texture is an artifact of the FIB process..... 69
Figure 36. Process flow diagram for chemical etching of a PV TEM foil. ..... 70
Figure 37. a) The etched surface of bottom of the pit as viewed Nomarski contrast microscopy (left), b) SEM cross-section of foil after 3.5 hours of etching (right). Foil thickness is 35 µm..... 71
Figure 38. The etched surface of bottom of the pit as viewed Nomarski contrast microscopy (left), SEM cross-section of foil after 4.0 hours of etching. Foil thickness is less than 2 µm. ..... 72

**List of Tables**

Table 1. Characteristics of symmetric reflections investigated for LMM InGaAs TPV cells. ..... 12
Table 2. Characteristics of asymmetric reflections investigated for LMM InGaAs TPV cell..... 13
Table 3. Geometric beam compression obtained for glancing exit reflections investigated. ..... 16
Table 4. Summary of results for single InPAs layers extracted fro the literature or measured using HRXRD, AFM or TEM. ..... 17
Table 5. Results for Sarnoff InPAs samples. ..... 20
Table 6. Summary of results for InPAs 3-step buffers analyzed. ..... 26
Table 7. Summary of structural parameters for 05-366a. ..... 33
Table 8. Summary of structural parameters for 1-956. ..... 34
Table 9. Summary of results for the strain relaxed InGaAs TPV cells analyzed. ..... 36
Table 10. Dislocation spacing for increasing threading dislocation spacing assuming a random distribution of threading dislocations i.e. $L = \rho_{td}$. ..... 40
Table 11. Identified dislocation selective etchants for InP, GaAs, and InGaAsP. ..... 42
Table 12. Description of TPV015 structure used for InGaAs etching studies. InGaAs contact and InPAs window layers were removed to look only at the InGaAs emitter layer. ..... 48
Table 13. Chemical treatments considered in the study of SiN/InGaAs interface formation and stoichiometry. ..... 63
Table 14. Treatments considered in the interface study. ..... 67

# 1 Scope of research

## 1.1 Introduction

Significant efforts to improve lattice-mismatched $In_xGa_{1-x}As$ thermophotovoltaics (TPV) grown on InP substrates have resulted in record TPV cell performance. Given the large mismatch between the substrate and the active device, these excellent results are both surprising and encouraging. In this approach, lattice mismatch is accommodated through a step graded $InP_yAs_{1-y}$ buffer, and the success of this technology is solely dependent on the buffer layer minimizing the threading dislocation density that would otherwise limit device performance. Despite the demonstrated success of this technology, there exists a large dispersion in TPV device performance from growth platform to growth platform as well as for devices on a single platform, which is believed to be due to incomplete optimization of buffer layer growth. Further optimization will require applied investigations that address the fundamentals of threading-dislocation formation and propagation during structure growth. When the information obtained from the studies on a variety of structures is analyzed a more complete picture of strain relaxation and dislocation generation in $InAs_yP_{1-y}$ buffers and $In_xGa_{1-x}As$ TPV devices will be obtained. This comprehensive understanding will enable the development of a more robust process that will allow a thorough optimization of TPV device performance.

Optimization of these TPV structures could be achieved through applied investigations of threading-dislocation formation and propagation. One approach would be to contrast step grading to continuously graded structures to optimize strain relief. The relationship between the rate that the composition, and the resulting strain, is varied determines if threading dislocations propagate through the device or benignly relieve the

misfit strain below the device as desired. The doping of the buffer structure is important for TPV monolithic interconnected module (MIM) development. Impurities, introduced as electrical dopants, can also impact the rate of dislocation nucleation and glide; thus, TPV device design is coupled to buffer layer optimization through doping. Dislocation propagation is also affected by surface topography. For example, surface roughness can result in the formation of localized dislocation groups, or "lock-ups" that are sessile and cannot contribute to layer relaxation.

No single technique can provide all the information necessary for buffer layer optimization. Several key materials characterization techniques are needed to provide the structural information necessary for these buffer-layer optimization studies. The capabilities applied include: (i) high resolution x-ray diffraction and reciprocal-space mapping, which gives the strain, composition, and crystallographic misorientation of relaxed buffer layers; (ii) electron microscopy techniques that are sensitive to structural properties of dislocations, and (iii) chemical decoration of threading dislocations to quantify dislocation densities. The combined suite of information obtained from these techniques gives a more complete picture of strain relaxation and dislocation generation in $InP_yAs_{1-y}$ materials, which should enable a more thorough optimization of TPV devices.

### 1.1.1 *Ex situ* Characterization of Strain and Composition

High-resolution x-ray diffraction (HRXRD), specifically the use of reciprocal space mapping, has provided significant insight into buffer layer relaxation. Reciprocal space mapping determines the composition and strain state for all layers in a multilayer buffer structure and provides structural feedback needed to accurately lattice-match the buffer layer to the overlying TPV device. Serially scanning, commercially available x-

ray diffractometers and scientific expertise in x-ray diffraction are readily available at SNL to execute these measurements.

One disadvantage of serially acquired maps is the long data acquisition times that are often needed. These time constraints can be avoided by developing a unique x-ray diffractometer that employs a position-sensitive detector (PSD) - at Sandia, we call this PSD-based technique "K-map". Use of a PSD, which accomplishes parallel detection of x-rays in $2\theta$, greatly reduces the time required to make a full two-dimensional (2-D) reciprocal-space map. The traditional serial scanning time for a reciprocal space map is reduced from $N \times M \times \Delta t$ to simply $M \times \Delta t$, where $\Delta t$ is the sampling time and M and N are the number of sampling points in rocking and detector angles, respectively. In favorable circumstances, the speed gained is in fact ~N, and since N~M~100, substantial gains in speed are possible. A tradeoff made when using K-map is reduced angular resolution in $2\theta$. This is of little consequence when examining the broad diffraction peaks characteristic of strain-relaxed materials, and K-map is particularly well suited to study of $InP_yAs_{1-y}$ step graded buffer layers.

### 1.1.2 Microscopic Characterization of Threading Dislocation Density

Plan-view transmission electron microscopy (TEM) provides a technique to determine total threading dislocation densities directly, while cross-sectional TEM allows inspection of individual layers in a multilayer structure, which enables evaluation of dislocation generation and propagation at interfaces. Cross sectional TEM provides some opportunity to image small numbers of dislocations in layers with very high dislocation densities, greater than $1 \times 10^8$ $cm^{-2}$. For the dislocation densities expected in InPAs buffers and InGaAs TPV cells, it will not be reasonable to depend on cross-sectional TEM to quantify threading dislocation density. While an excellent scientific tool, sample

preparation for TEM is difficult and time consuming. TEM will be invaluable for early optimization of $InP_yAs_{1-y}$ and can be used to evaluate more rapid techniques for quantifying dislocation densities. A technique utilizing the differences in chemical etch rates of InP relative to InPAs was developed to reduce the time required for sample preparation.

### 1.1.3 Chemical threading dislocation identification.

Because of its labor-intensive character, TEM is unsuited for routine process optimization, and alternative techniques that provide more rapid feedback on threading-dislocation density are needed. Etches have been developed in other III-V materials that preferentially decorate dislocation cores with etch pits. These etching techniques have enabled rapid threading dislocation density measurements using optical microscopy over large areas to count the pit density (EPD). The limited success of this technique when applied to $InP_yAs_{1-y}$ is due to the convolution of the surface roughness, due to the misfit dislocation network, with the threading dislocations. Our approach has been to use short times to limit the reaction forming the pit and image the surface with atomic force microcopy (AFM) to improve the resolution between pits. EPD techniques will need to be calibrated against results from plan view TEM, which has a fundamental sensitivity to the crystal discontinuity associated with a threading dislocation. Dislocation decorating etches have been developed for other III-V semiconductors and these recipes are available in the literature. Electron beam techniques for dislocation identification and characterization.

## 1.2 Summary

The optimization of $InAs_yP_{1-y}$ buffer layers and the resulting $In_xGa_{1-x}As$ TPV devices can be impacted positively a coordinated and complete characterization of the strain, composition and threading dislocation density. The strain and dislocation density of a variety of structures can be correlated with growth methods and device performance to advance the development of a robust TPV technology based on lattice- mismatched InP/InAsP/InGaAs structures.

## 2 *Ex situ* characterization of strain and composition using high resolution x-ray diffraction reciprocal space mapping.

### 2.1 Introduction

X-ray diffraction techniques are capable of providing information about strain, composition, and tilt of epitaxial layers. This is critical information since the InGaAs TPV cell must be closely lattice matched to the underlying InPAs buffer to obtain any reasonable performance. Preliminary evaluation of different symmetric and asymmetric reflections available was carried out to determine which reflections would provide the best angular resolution and highest absolute accuracy. Serial scans around the desired reciprocal lattice points were performed, mapping out the intensity as a function of the radial ($2\Theta/\Omega$) and transverse ($\Omega$) angles. The analysis of the poles measured in the map to give strain and composition of the layers was performed for several samples provided by Sarnoff Laboratories and MIT's Lincoln Laboratories. Three general categories of samples were evaluated: single InPAs layers on InP, InPAs buffers on InP, and InGaAs TPV cells on InPAs buffers.

A survey of the available equilibrium models on strain relaxation of epitaxial thin films was performed to place the results for the single InPAs layers in context and provide insight into InPAs film relaxation. The transverse diffuse scatter from slightly relaxed InPAs layers was evaluated and correlated to the linear density of misfit dislocations obtained from AFM and planview TEM analysis. These results provide insight into the initial evolution of crystallographic tilt in InPAs layers.

General results for InPAs buffers are presented and discussed. The transverse linewidths for two InPAs buffer was measured using symmetric and quasi-symmetric reflections and the results were analyzed to give the degree of tilt and twist in the sample,

which is related to the threading dislocation density. The values obtained from linewidth analysis are compared to the density of surface features measured in AFM and the threading dislocation density observed in cross-sectional TEM. The postulated limitations on this technique are discussed.

The evaluation of the strain state of InGaAs TPV devices grown on the InPAs buffer is necessary feedback to know how the epitaxy process should be adjusted to lattice match the TPV cell to the buffer. General results are presented and some of the limitations of using RSMs for evaluation are discussed.

## 2.2 Preliminary evaluation of available reflections

A survey of preferred crystallographic reflections for evaluating LMM TPV was performed during early sample characterization. The issues associated with the measurements were: a) resolution of layers in the structure i.e. can we see the layers of interest, b) maximizing signal from a layer, c) evaluating absolute composition error for possible reflections. Table 1 and 2 below summarize the evaluation of relevant reflections.

**Table 1. Characteristics of symmetric reflections investigated for LMM InGaAs TPV cells.**

| Reflection | Substrate Intensity (Open detector) [kcps] | Cell Intensity (Open detector) [kcps] | Θ Angular Separation [(° in Θ)/(Δd/d)] | Out of Plane Strain Error [-/ΘΔ] |
|---|---|---|---|---|
| (004) | 148 | 292 | 0.62 | 1.6 |
| (006) | 60 | 7 | 1.28 | 0.8 |

**Table 2. Characteristics of asymmetric reflections investigated for LMM InGaAs TPV cell**

| Reflection | Substrate Intensity Glancing Incidence (Open detector) [kcps] | Cell Intensity Glancing Incidence (Open detector) [kcps] | Θ Angular Separation [°/(Δd/d)] | In-Plane Strain Error [-] | Absolute Composition Error [%] |
|---|---|---|---|---|---|
| (115) | 94 | 87 | 0.93 | 1.3E-3 | 4.0 |
| (224) | 0.1 | 60 | 0.84 | 3.2E-4 | 1.0 |
| (335) | 29 | 47 | 1.69 | 1.3E-4 | 0.4 |
| (444) | 10 | 110 | 2.19 | 6.0E-5 | 0.2 |

For symmetric reflections the (004) has superior intensity to the (006), making it preferred for reciprocal space mapping (RSM). The (006) reflection has advantages for peaks that overlap in the (004) because it provide larger angular separation. (006) is not useful for serially-acquired RSM due to the low count rates, but 2Θ/Ω linescans taken with this reflection can be fit using Gaussian lineshapes to determine peak positions that can't be evaluated otherwise. (006) also has the advantage that it is quasi-forbidden for InGaAs, but allowed for InP and InPAs. This means that the intensity of the InGaAs TPV cell is reduced relative to that of the InP substrate and the InPAs buffer layers making peak identification and fitting easier.

For asymmetric reflections only the (224) has technical difficulties in finding the substrate peak. This is not an issue for InPAs buffers, only for TPV cells. Another issue identified was that the (115) has slightly superior angular resolution than the (224). Sensitivity analysis around the composition $InP_{0.32}As_{0.68}$ to evaluate the accuracy of the possible reflections clearly shows that the (115) is not the preferred reflection. The

absolute error in composition is 4 percent, unacceptably high for process control. The other reflections that provide sufficient substrate intensity for alignment and low absolute compositional error are the (335) and the (444). The (444) reflection should provide superior resolution by separating out closely spaced peaks similar to the (006). This reflection is limited by low intensity for layers of the buffer structure. The (335) reflection was identified as a reasonable compromise to the (444) for future characterization.

The overall intensity of features is another issue that was addressed. It is common in RSM to use a third analyzer crystal before the detector to limit the angle sampled. This severely limits the count rate measured and the ability to find weak signals from the underlying buffers. For lattice relaxed layers the angular breadth (FWHM) of peaks is so large that an analyzer crystal does not provide any enhancement of the angular resolution. A collimator or slit can be used instead of the analyzer crystal to limit the detector's acceptance angle for the diffracted beam. No change in the methodology for obtaining the symmetric reflections are needed, but for the asymmetric reflections the diffracted

$$x_0 = \frac{w_0}{\tan(2\Theta)}$$

$$x_1 + x_0 = \frac{w_0}{\tan(\omega)}$$

$$x_1 = \frac{w_0}{\tan(\omega)} - \frac{w_0}{\tan(2\Theta)}$$

$$w_1 = x_1 \sin(2\Theta)$$

$$w_1 = \left(\frac{w_0}{\tan(\omega)} - \frac{w_0}{\tan(2\Theta)}\right)\sin(2\Theta)$$

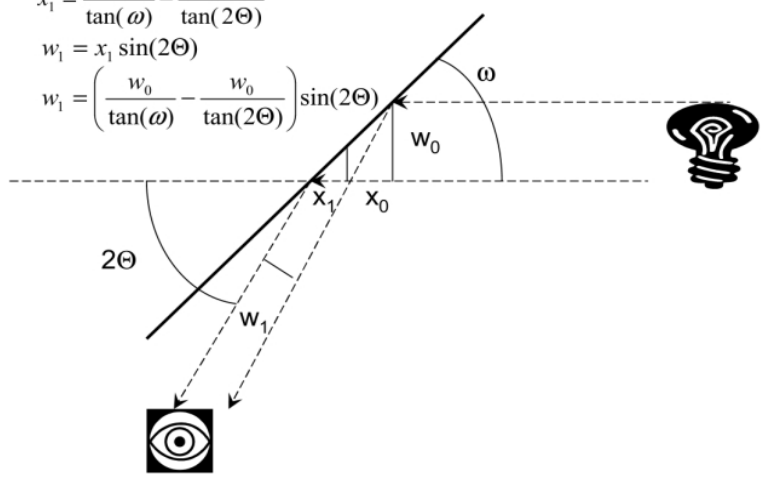


**Figure 1 Geometry showing the spatial beam compression for glancing exit geometry. Derivation is included.**

beam is expanded for glancing incidence geometry and compressed for glancing exit geometry. This is illustrated in Figure 1 showing the geometry resulting in beam compression. Using an expanded beam width with a slit further reduced the signal detected. A compressed beam width provides higher intensity if the width of the incident beam is matched to the width of the collimator. Too large of an incident beam just spreads the diffracted intensity out over a larger width. The width of the incident beam can be adjusted to get close coupling to the detector and maximizing the detected signal. Table 3 shows the beam compression for the asymmetric reflections evaluated in the glancing exit geometry. Experimentally the width of the incident beam is set by adjustable knife-edge slits and the width of the exiting beam is set by the collimator.

**Table 3. Geometric beam compression obtained for glancing exit reflections investigated.**

| | | | | |
|---|---|---|---|---|
| h | 1 | 2 | 3 | 4 |
| k | 1 | 2 | 3 | 4 |
| l | 5 | 4 | 5 | 4 |
| W1 [mm] | 0.1875 | 0.1875 | 0.1875 | 0.1875 |
| W0 [mm] | 0.35075 | 2.18916 | 0.56545 | 0.87493 |
| W1/W0 [-] | 0.53456 | 0.08565 | 0.3316 | 0.2143 |

## 2.3 Strain and composition determination using HRXRD/RSM

The primary focus of the HRXRD work was support for Sarnoff Laboratories and MIT's Lincoln Laboratories TPV growth effort. Three classifications of samples were analyzed using HRXRD during this effort: single InPAs layers on an InP substrate, InPAs buffers consisting of a numbers of layers with increasing amounts of InAs in InPAs, and InGaAs TPV cells on a InPAs graded buffer.

### 2.3.1 Single InPAs layers on InP

The easiest and most scientifically interesting structures analyzed were single layers of InPAs with a uniform composition. Due to there simplicity, these structures enable the fundamental structural properties of InPAs to be investigated. The available literature on InPAs is relatively spare compared to better studied III-V alloy systems, such as InGaAs and InAlAs. Some of the models applied to these systems can be used to evaluate the InPAs systems. Table 4 below summarizes the relevant characteristics and measured parameters for single InPAs layers on InP substrates measured and relevant studies from the literature.

**Table 4. Summary of results for single InPAs layers extracted fro the literature or measured using HRXRD, AFM or TEM.**

| Thickness [Å] | Growth rate [Å/second] | InAs composition [%] | Coherency strain to InP [-] | Relaxation [%] | Residual strain [-] | Equilibrium critical thickness [Å[ | Reference or sample number/source (measurement technique) |
|---|---|---|---|---|---|---|---|
| 400 | 1.7 | 50 | 0.0159 | 65 | 0.0056 | 57 | 1 (XRD) |
| 4000 | 1.7 | 50 | 0.0159 | 94 | 0.0010 | 57 | 1 (XRD) |
| 19000 | 2.2 | 5 | 0.0016 | 60 | 0.0006 | 937 | 2 (XRD) |
| 19000 | 2.2 | 10 | 0.0032 | 70 | 0.0010 | 414 | 2 (XRD) |
| 10000 | N/A | 50 | 0.0159 | 76.9 | 0.0037 | 57 | 3 (XRD) |
| 3500 | 2.5 | 18 | 0.0058 | 46.5 | 0.0031 | 204 | 05-314c, MIT-LL (XRD) |
| 3500 | 2.5 | 17.9 | 0.0057 | 64 | 0.0021 | 204 | 05-331c, MIT-LL (XRD) |
| 3500 | 2.5 | 32.6 | 0.0104 | 78.6 | 0.0022 | 96 | 05-341c, MIT-LL (XRD) |
| 1600 | 5 | 14.3 | 0.0046 | 9 | 0.0042 | 276 | VE196, Sarnoff (AFM) |
| 2500 | 5 | 13.6 | 0.0044 | 63 | 0.0016 | 276 | VE195, Sarnoff (TEM) |
| 190 | 2.1 | 48 | 0.0153 | 1.4 | 0.0150 | 60 | 4 (TEM) |
| 190 | 2.1 | 53 | 0.0168 | 1.9 | 0.0165 | 53 | 4 (TEM) |
| 190 | 2.1 | 66 | 0.0209 | 1.3 | 0.0206 | 39 | 4 (TEM) |

Individual InPAs layers have very limited relaxation. The amount of residual strain retained by the single layer lies between 2 x $10^{-3}$ and 3 x $10^{-3}$ elastic in-plane strain (EIPS) for 350 nm single layers. Comparing 05-314c to 05-341c, the residual strain retained by the film decreases slightly as the initial coherency strain is increased. More strain is retained by undoped InPAs layers (05-314c) compared to similar composition and thickness Te-doped films (05-331c). This supports the argument that Te-doping is important to obtain the optimum InPAs buffer relaxation.

### 2.3.2 Equilibrium models of layer relaxation

It is readily apparent from Table 4 that the thicker a film is the more relaxed it will be. Three regimes of layer relaxation can be modeled using different theories. The first is the coherent, or psuedomorphic, regime. This is characterized by all of the constant coherency strain energy being absorbed by a tetragonal distortion of the layer. These limits are given as the horizontal lines on the left side of Figure 1 below. The thickness tolerated by the film decreases as the InAs composition of the film increases from 10% InAs to 50 % InAs in Figure 1. The second regime is associated with strain relief by dislocation generation in the film. The energy required to form a misfit dislocation largely determines the slope of the curve. Figure 1 shows three diagonal lines for three specific dislocation energies: 3E-4 ergs/cm, 4.5E-4 ergs/cm, and 6E-4 ergs/cm.[5] The third regime is associated with limited relaxation due to the difficulty of injecting new dislocations into the existing dislocation array. This effect is more pronounced for films with high InAs compositions (50 percent InAs), but still occurs for lower InAs compositions (10 percent InAs).[6] This regime is depicted by the shallow curves on the right side of Figure 1.

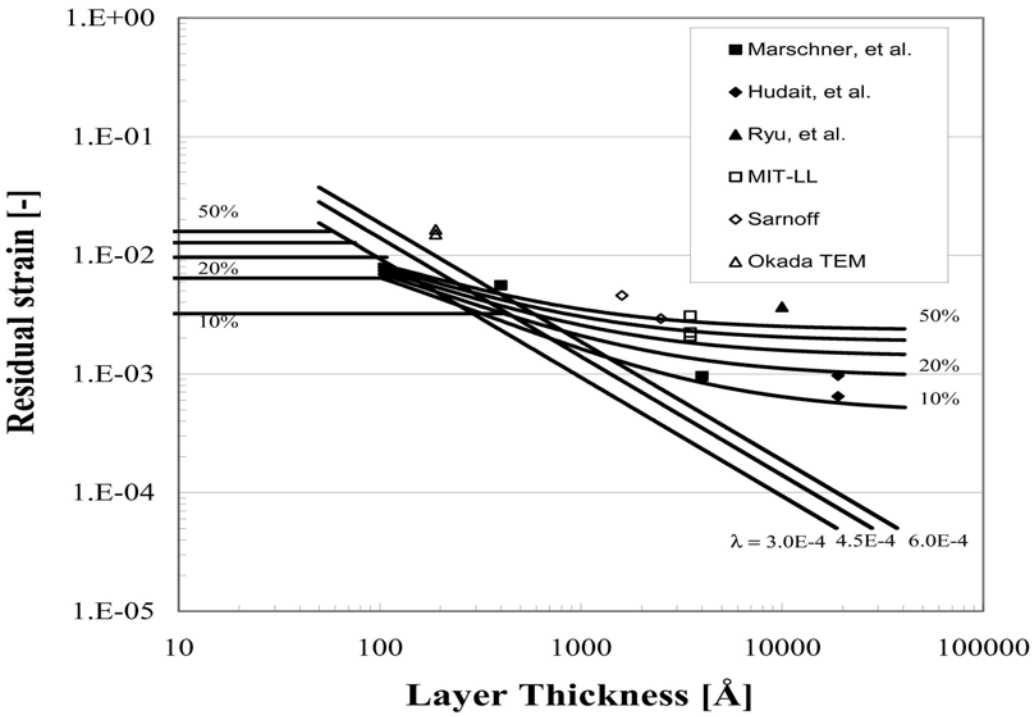


**Figure 2. Residual strain in various single layers either measured in this study or available in the literature.**

As with other III-V alloys, InPAs shows a delayed onset of relaxation. The experimentally observed critical thickness for $InP_{0.86}As_{0.14}$ is close to 1600 Å, over five times the equilibrium critical thickness. For $InP_{0.52}As_{0.48}$ the experimental critical thickness is closer to 190 Å, approximately three times the equilibrium value. Limited agreement of the residual strain. Clearly equilibrium theories of strain relaxation are not quantitative for InPAs alloys for the thicknesses relevant in TPV buffer layers.

### 2.3.3 Transverse linewidth analysis of single InPAs heterostructures

Two samples grown by Sarnoff Laboratories were analyzed to gain insight into the relaxation of the first InPAs buffer layer. The films were approximately 160 nm and 250 nm thick estimated from interference oscillations from HRXRD. Table 5 shows that most of the coherency strain is retained by the films. The relaxation exhibited by these

films is similar in magnitude to the strain sensitivity of the technique, approximately 2 x $10^{-4}$.

**Table 5. Results for Sarnoff InPAs samples.**

| Sample Number | Thickness [nm] | Composition | EIPS Parallel strain [ppm] | Perpendicular strain [ppm] | Coherency strain to InP [ppm] |
|---|---|---|---|---|---|
| VE195 | 250 | 14.3 | 4269 | -4724 | 4600 |
| VE196 | 180 | 13.6 | 4237 | -4689 | 4400 |

The equilibrium critical thickness for these films is approximately 40 nm, suggesting these films are metastable and should have more relaxation than predicted by analysis of the 2Θ angular position of the substrate and epilayer peaks. Transverse scans through the epilayer Bragg peak were performed to evaluate the diffuse scattering present at the early stages of layer relaxation. The linescans from 0° and 90° azimuths are shown below for both samples.

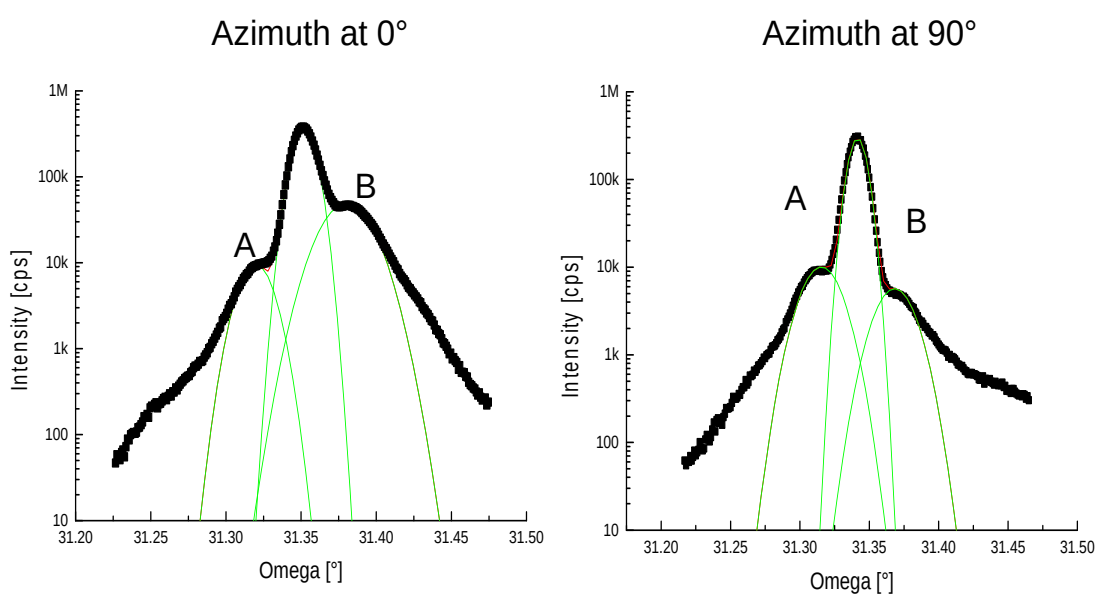


**Figure 3. Transverse scans at 0° and 90° azimuths for VE195**

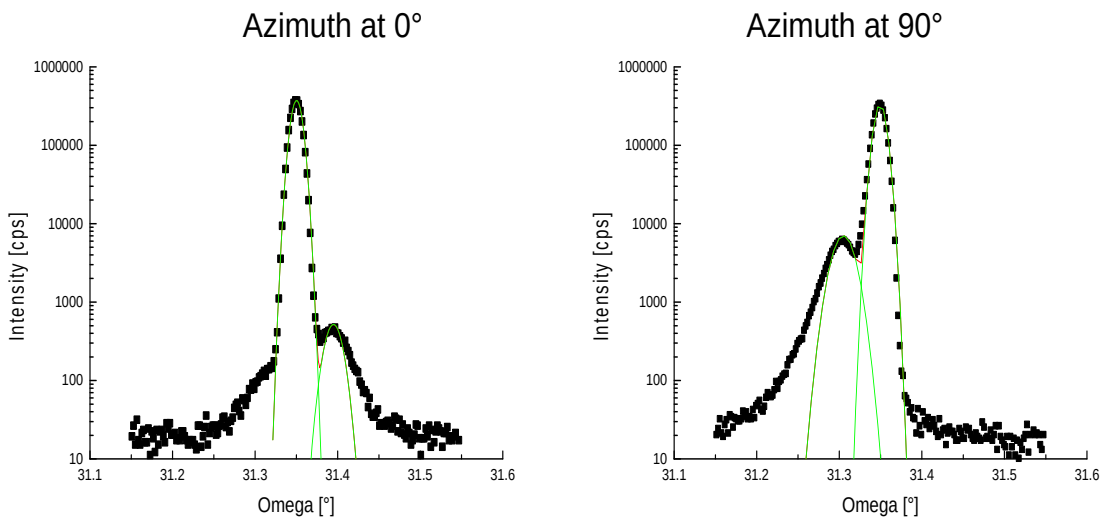


**Figure 4. Transverse scans at 0° and 90° azimuths for VE196**

The relative diffuse intensity on each side of the Bragg peak is proportional to the linear density of misfit dislocations. Two orientations of the Burger's vector can be observed for each azimuth depending on the film's relaxation. However, the distribution of these orientations is not equal in magnitude, resulting in a net tilt of the epilayer with respect to the substrate. Rotation about the azimuth by 90° allows investigation of the relative concentration of dislocation types in the sample. Dislocations can have indium atoms around their core, termed β dislocations, or arsenic and phosphorus atoms in the core, termed α dislocations. The Gaussian fits to the Bragg peak and the diffuse peaks given in Figures 3 and 4 represent an attempt to quantify this intensity. For the thinner sample, VE196, the dislocations formed have nearly a single Burgers vector orientation with a slight asymmetry of the dislocation type. It is not possible from the data available to determine which core type dominates, but theoretical arguments would suggest that the first dislocations to form in III-V materials are α dislocations. The thicker sample, VE195, shows both core types. In addition, the diffuse scatter for VE195 is beginning to

merge with the Bragg peak. Figure 5a shows an AFM image of the surface of VE196 that was taken scanning 45° to the orthogonal crystallographic axis. The diagonal lines are believed to be linear misfit dislocations intersecting the surface. The linear misfit density suggest for VE196 is 1400 $cm^{-1}$, corresponding to a mean misfit spacing of 7 µm. Figure 5b is a planview TEM micrograph showing a much higher dislocation density between 6 x $10^6$ $cm^{-1}$, which corresponds to dislocation spacing of 0.2 µm. The conclusions from this study suggest that InPAs, like other mismatched III-V materials, has a substantial region of metastablity where less relaxation occurs than predicted by equilibrium models. This study also highlights that analysis of 2Θ angle position does not give the correct answer for the residual strain for thin films with low coherency strains.

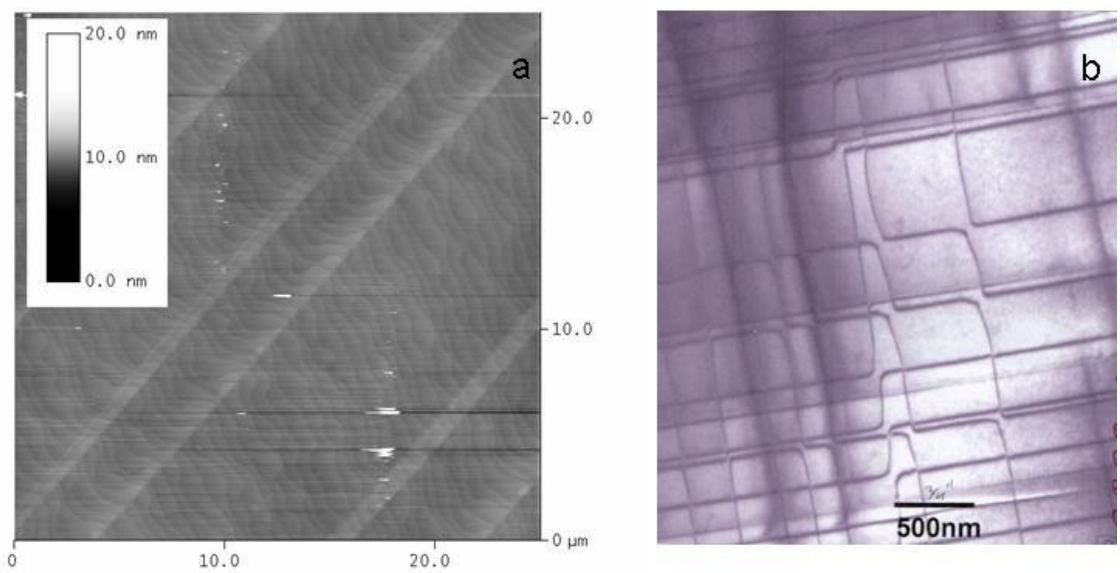


**Figure 5. Microscopy quantifying the linear density of misfit dislocations in VE196 and VE195. a) AFM micrograph of surface showing linear misfit intersection the surface. The density is 1400 $cm^{-1}$, giving a mean spacing of 7 µm. b) TEM micrograph showing the misfit dislocation network. The density is about 6 x $10^4$ $cm^{-1}$, giving a mean spacing of 0.2 µm.**

## 2.4 InPAs buffers

The goal of the buffer layer is to relax as much of the mismatch strain through the formation of misfit dislocations that lie in the sample plane. Unfortunately, the formation of misfit dislocations requires the formation of threading dislocations, propagating typically 60° to the growing surface. The threading dislocations can be deleterious to high performing InGaAs TPV cells grown on top of the buffer by providing non-radiative recombination centers for minority carriers. The interface between the InPAs buffer and the InGaAs TPV cell needs to be lattice matched within the resolution of HRXRD to avoid generating new threading dislocations.

The standard buffer analyzed in this program was a 3-step buffer with targets of 0.7 µm $InP_{0.84}As_{0.16}$, 0.7 µm $InP_{0.72}As_{0.28}$, and 1.4 µm $InP_{0.68}As_{0.32}$, grown in increasing composition. The top $InP_{0.68}As_{0.32}$ layer was thicker than the others because this also serves as the lateral conduction layer. Other buffer designs may be preferred to the 3-step buffer, but because the program emphasized reproducing existing work, little research was done on alternative buffer designs. One structure was grown using a linearly graded buffer starting with layer of $InP_{0.94}As_{0.06}$, increasing the As composition linearly, and ending with a thick layer of $InP_{0.64}As_{0.36}$. Another buffer grown at the National Renewable Energy Laboratory (NREL) was a five step structure that targeted a different final lattice constant than the other structure evaluated. The analysis of the samples using alternative grading schemes will be contrasted to the 3-step structure.

### 2.4.1 3-step InPAs buffers

Nine InPAs buffers were analyzed during this project. Most of the buffers came from MIT-Lincoln Laboratories, but two were grown at Sarnoff Laboratories, and one

was grown by Emcore Photovoltaics. Figure 6 shows representative RSM for the (004) and (335) reflections for sample 05-360a.

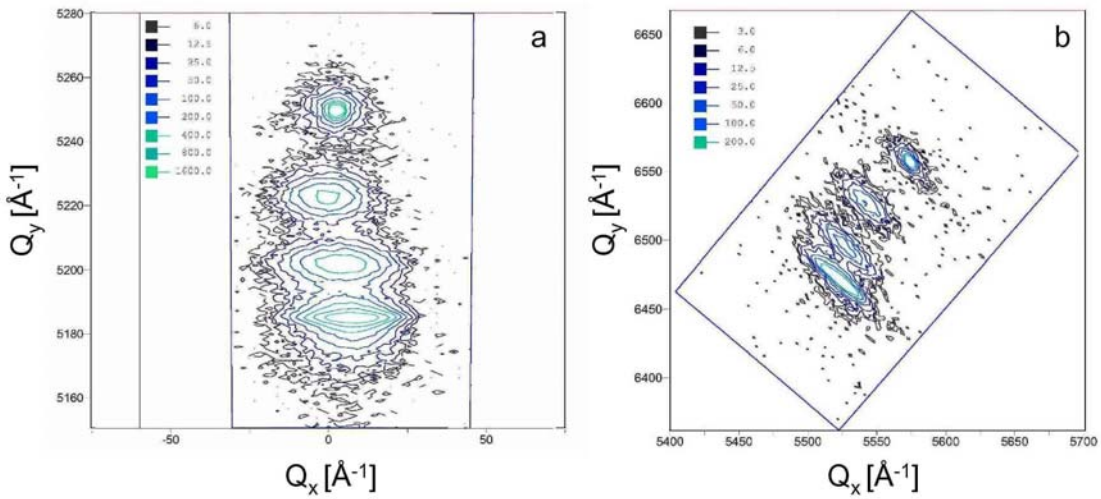


**Figure 6. Representative RSM for sample 05-360a showing the features measured. a) (004) reflection and b) (335) reflection.**

All three layers grown and the InP substrate were measured for (004) and (335) reflections. The shift of the epilayer peaks off the radial direction through the substrate peak is the tilt introduced by asymmetric α- and β- dislocation injection. Table 6 summarizes the results for the buffers analyzed. All the buffers have nearly complete relaxation of the bottom two layers of the structure. The top layer is approximately 90 percent relaxed in all cases. Compared to mixed group III alloy buffers, grown in InGaAs and InAlAs, the low residual strains observed for InPAs and one of the key features of this material system. Generally, mixed group III buffers seem to retain much more residual strain. This feature would not be expected from looking at single layers of InPAs, because they seem to retain a similar amount of residual strain as mixed group III

buffers would. Clearly subsequent layers grown on top of the previous either generate new dislocations in the existing film or provide sufficient stress to drive the propagation of existing dislocations. The exact mechanism for this additional relaxation was not identified in our studies.

Another observation is that the 2Θ full width at half maximum for VE083 and VE208a are two to three times larger than other samples. Two differences for these samples should be noticed. Both of these samples were heavily Zn-doped and both showed signs of tensile InGaP being deposited at the nucleation of growth. The effect of a tensile nucleation layer is not known, but this condition would not be considered optimum. The effect of the Zn doping can be speculated based on measured dislocation velocities in n- and p-type InP.[7] The dislocation velocity in Zn-doped InP is four orders of magnitude lower for α-dislocations than in S-doped InP. β-dislocations have approximately the same velocity in either Zn- or S-doped material. This suggests that promoting the formation of α-dislocations is important for optimal buffer function. Since at growth temperature the electrical conductivity type is not relevant, the effect of the dopant can only be mechanical, modifying the yield stress of the different slip systems available for strain relief.

**Table 6. Summary of results for InPAs 3-step buffers analyzed.**

| Sample No. (miscut from 100 surface) | InAs Composition $1^{st}/2^{nd}/3^{rd}$ [%] | Coherency strain to InP $1^{st}/2^{nd}/3^{rd}$ [%] | Doping element and level [$cm^{-3}$] | (004) 2Θ FWHM $1^{st}/2^{nd}/3^{rd}$ [°] | (004) Ω FWHM $1^{st}/2^{nd}/3^{rd}$ [°] | Tilt $1^{st}/2^{nd}/3^{rd}$ [°] | Residual strain $1^{st}/2^{nd}/3^{rd}$ X $10^4$ [-] | Relaxation $1^{st}/2^{nd}/3^{rd}$ [%] |
|---|---|---|---|---|---|---|---|---|
| VE083 | 16.6 | 0.53 | Zn = 1 x $10^{18}$ | 0.1186 | Not | Not | 0 | 107.8 |
| (±0.2° | 29.7 | 0.95 | | 0.1004 | evaluated | evaluated | 3 | 96.5 |
| miscut) | 33.6 | 1.07 | | 0.0440 | | | 10 | 90.3 |
| VE208a | 15.3 | 0.49 | Zn = 1 x $10^{18}$ | 0.181 | 0.232 | -0.12 | 3 | 94.7 |
| (±0.2° | 26.5 | 0.85 | (level assumed) | 0.354 | 0.336 | -0.14 | 13 | 84.8 |
| miscut) | 31.8 | 1.03 | | 0.159 | 0.293 | -0.14 | 13 | 87.3 |
| 05-360a | 14.3 | 0.46 | Te | 0.094 | 0.153 | 0 | -2.2 | 104.8 |
| (±0.2° | 26.1 | 0.84 | | 0.087 | 0.188 | 0.04 | -1.7 | 102.4 |
| miscut) | 29.4 | 0.95 | | 0.038 | 0.175 | 0.08 | 8.1 | 91.4 |
| 05-360b | 14.1 | 0.46 | Te | 0.077 | 0.111 | -0.06 | 3.4 | 92.4 |
| (2° miscut | 26.8 | 0.86 | | 0.058 | 0.096 | 0 | 1.5 | 98.2 |
| toward [110]) | 34.8 | 1.12 | | 0.072 | 0.197 | 0.02 | 12.3 | 89.0 |
| 05-360c | 14.1 | 0.46 | Te | 0.107 | 0.168 | -0.04 | 3 | 92.4 |
| (±0.2° | 26.8 | 0.86 | | 0.098 | 0.172 | -0.06 | 1.5 | 98.2 |
| miscut) | 34.8 | 1.12 | | 0.097 | 0.135 | -0.08 | 12.3 | 89.0 |
| 05-362a | 18.1 | 0.58 | Undoped | 0.096 | 0.191 | -0.09 | -0.3 | 100.5 |
| (±0.2° | 27.7 | 0.89 | | 0.075 | 0.198 | -0.09 | 1.2 | 98.6 |
| miscut) | 32.8 | 1.06 | | 0.041 | 0.180 | -0.08 | 8.7 | 91.7 |
| 05-362c | 17.6 | 0.57 | Undoped | 0.106 | 0.157 | -0.06 | -0.4 | 100.9 |
| (±0.2° | 27.4 | 0.88 | | 0.091 | 0.169 | -0.06 | 0.8 | 99.0 |
| miscut) | 32.2 | 1.03 | | 0.063 | 0.160 | -0.06 | 8.6 | 91.6 |
| 5ey021-3 | 16.1 | 0.51 | Te = 1 x $10^{19}$ | 0.107 | 0.131 | 0.02 | 0.9 | 98.2 |
| (2° miscut | 26.7 | 0.85 | | 0.098 | 0.142 | -0.06 | 0.7 | 99.2 |
| toward [110]) | 32.3 | 1.03 | | 0.069 | 0.135 | -0.06 | 7.0 | 92.8 |

#### 2.4.1.1 Transverse width analysis of 3-step buffers

Extensive literature exists attempting to correlate x-ray peakwidth measurements to threading dislocation densities. The original literature on this subject was developed for highly defective metal samples with dislocation densities between 4 x $10^8$ and 6 x $10^{10}$ $cm^{-2}$.[8,9,10,11] This relationship was brought into thin film semiconductor work as a measure of sample quality, especially for samples that contain dislocations, as in the case of strain-relaxed buffers or heavily mismatched epitaxy.[12,13,14] It has been recognized through dynamic simulation of dislocation scattering that for low misfit systems, approximately 1% strain, the peakwidth does not correlate in a quantitative manner to the dislocation density.[15] The threshold dislocation density or range of densities over which the correlation is applicable has not been identified. For GaN on $Al_2O_3$ where the densities are between 1 x $10^8$ and 1 x $10^{10}$ $cm^{-2}$, the correlation has been shown to apply reasonably well for edge dislocations, but not as well for screw dislocations. This success suggested that InPAs 3-step buffers might be another suitable system to study where x-ray peakwidth correlations can be applied or why they might fail.

Three contributions to the transverse peakwidth, the tilt peakwidth ($\Gamma_y$), the twist peakwidth ($\Gamma_z$), and the correlation length, that can be thought of as an average domain size (L), are considered in the model. These three components are illustrated in Figure 7 for the geometry used. The linewidth, $\Gamma_{hkl}$, is measured as a function of interplanar angle, $\chi$, using a combination of symmetric and quasi-symmetric, or skew, diffraction conditions. The results were fit to the expression:

$$\Gamma_{hkl}^{n} = (\Gamma_y \cos\chi)^n + (\Gamma_z \sin\chi)^n + \left[\frac{2\pi / L}{K_{hkl}}\right]^n$$

Where $K_{hkl}$ is the magnitude of the diffraction vector for the (hkl) reflection. The value of n was taken as 2.

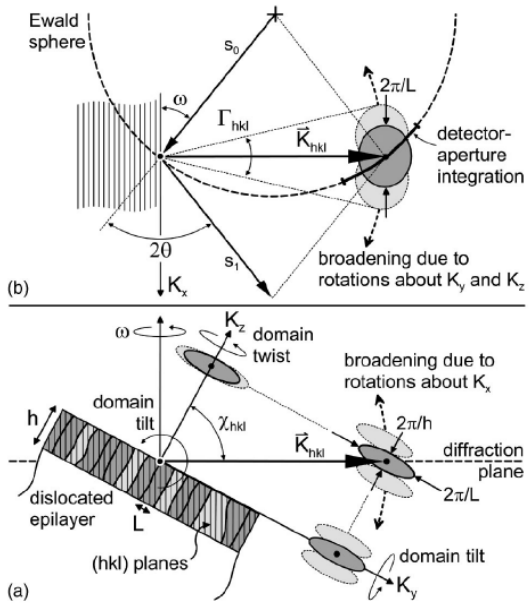


**Figure 7. Illustration of the diffraction geometry used for x-ray linewidth measurements and the source of the tilt and twist components of the linewidth about $K_x$ and $K_z$, respectively, and the finite size effects associated with the correlation length L. a) Shows the cross-sectional view of the geometry, b) shows the plan view.[14]**

Figure 8 shows the fit obtained for VE159. For the fit generated $\Gamma_y$ = 0.149°, $\Gamma_z$ = 0.041°, and L > 800 nm. To relate the linewidth components to the dislocation densities the expression:

$$\rho = \frac{\Gamma^2}{4.36b^2}$$

developed in reference 10 is used. Using a screw Burgers vector magnitude of 2.1 Å with the tilt component a screw dislocation density of 3.5 x $10^9$ $cm^{-2}$ is obtained. Using an

edge Burgers vector of 3.6 Å with the twist component, an edge dislocation

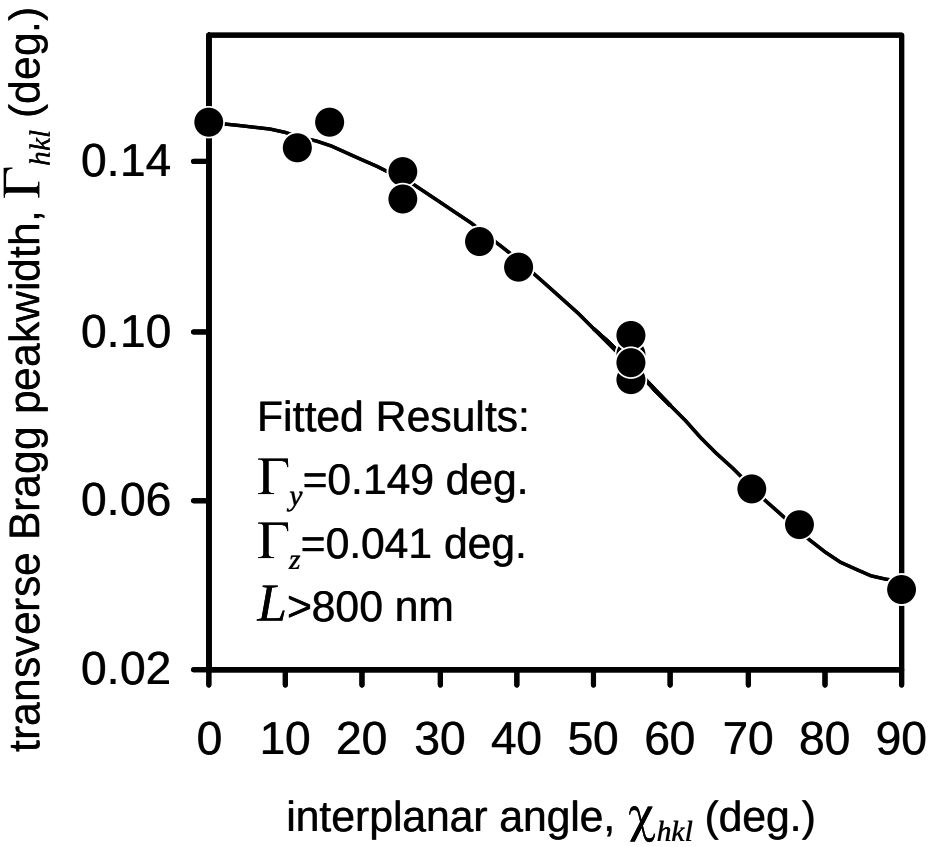


**Figure 8. Transverse peakwidth measurements as a function of interplanar angle with a fit to extract the tilt and twist components of the linewidth. The correlation length cannot be evaluated from the measurements, suggesting the domain size is large.**

density of 9.1 x $10^7$ $cm^{-2}$ was obtained. These values can be compared to measured values of the dislocation density or surface pit measurements of this film. Cross-sectional TEM (XTEM) was performed at KAPL, Inc. on VE159. Cross-sectional measurements are not the best way to count dislocation densities, but if dislocations are observed the density should be substantial. Several measurements of small regions in the top InPAs buffer set the dislocation density between 2.9 x $10^7$ and 4.2 x $10^8$ $cm^{-2}$. Atomic force microscopy (AFM) images of the surface of VE159 show a high density of small pits

with a density exceeding 1.1 x $10^8$ $cm^{-2}$. The value obtained for the screw dislocation density is almost an order a magnitude higher than the upper end measurement obtain from XTEM suggesting the correlation to the peakwidth analysis is poor. The value obtained for the edge dislocation density is significantly better, lying between the limits set by XTEM and falling very close to the value of the pit density observed with AFM. As mentioned above the same model was applied to III-nitride materials, with reasonable agreement for the twist component and poor agreement for the tilt component. The difference to III-nitride materials was that tilt component underestimated the screw dislocation density, whereas for InPAs the tilt component is overestimating the expected screw dislocation density.

Understanding the necessary sample conditions for peakwidth-based techniques to provide useful information and where they will not cannot be extrapolated from a single sample. However, one speculation can be hypothesized in advance of additional data. For metal samples and heavily dislocated films like GaN the dislocation density is homogeneous throughout the volume of the sample or film as shown in Figure 9a. The sample is characterized by a high density of dislocation loops near the substrate/film interface and a high density of dislocations in the uniform thick film. The x-ray scattering, observed as the peakwidth, is dominated by the threading dislocations in the uniform film and the interface dislocations contribute only a small about to the scattering. The high dislocation density correlates to a low value of the correlation length. The scattering from a thin film (Figure 9b) with few dislocations is dominated by the misfit dislocation array at the substrate epilayer interface. In this case peakwidth based techniques should give a dislocation density that is much larger than really exists in the

film. Scattering from a thick film with many dislocations (Figure 9c) still has a scattering component due to the misfit dislocation array, but the linewidth begins to become dominated by scattering from dislocation in the homogeneous film. This begins the regime where peakwidth based techniques might be applied to dislocation density measurements. From a device optimization standpoint, peakwidth based techniques might not be the best correlation, because the material with the best performance might also have peakwidths dominated by the interface misfit array and not dislocation distributed in the relevant layers.

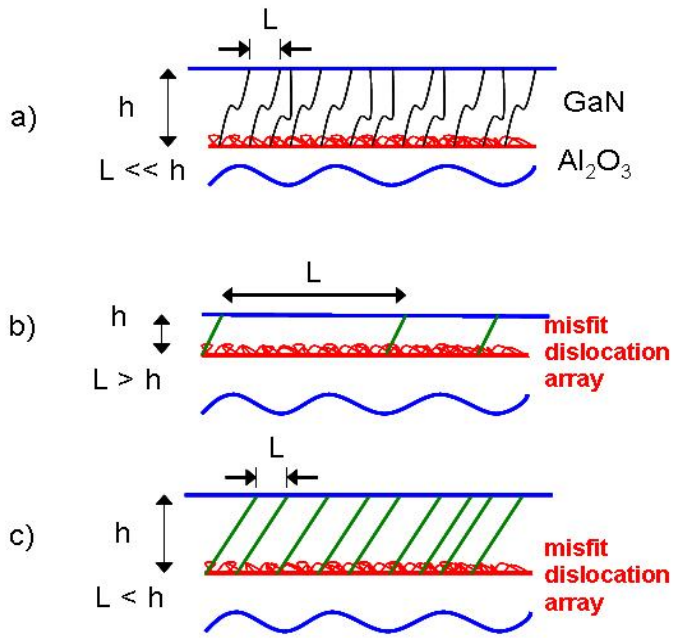


**Figure 9. Schematics showing the different regimes where peakwidth techniques might and might not apply. a)III-nitrides on $Al_2O_3$ have a high density of dislocations in the film volume resulted in a reasonable correlation b)The scattering from a thin film with few dislocations is dominated by the misfit dislocation array, and might produce unreasonably high dislocation densities from a peakwidth analysis. c)Scattering from a thick film with many dislocations should produce dislocation densities from the peaklinewidth analysis that agree more favorably.**

### 2.4.2 Linearly graded buffer layers

While the strain relaxation exhibited by the 3-step buffer layers is remarkable, step graded buffers do not provide a continuous stress on dislocations. The stress is highest as

the next layer is deposited coherently on the underlying layer. As the layer relaxes this stress is reduced, limiting the rate at which dislocations move. Linearly graded buffers provide a constant force on dislocations and therefore should be more efficient in getting the maximum relaxation for the minimum density of threading dislocations.

MIT Lincoln Laboratories sample 05-366a was grown to see what the effect of a linear grade would be. After a 100 nm InP:Si buffer layer the structure was started with a 0.5 µm $InP_{0.94}As_{0.06}$:Te layer of uniform composition. After the $InP_{0.94}As_{0.06}$ layer the As composition in the film was increased linearly over 1.6 µm while maintaining Te doping. The structure was capped with uniform composition $InP_{0.64}As_{0.36}$:Te layer 0.7 µm thick. The total thickness of the buffer is comparable to the 3-step buffers evaluated. This sample also had 1.0 µm layer of $In_{0.68}Ga_{0.32}As$ lattice matched to the top $InP_{0.64}As_{0.36}$ layer. RSMs for the symmetric (004) and asymmetric (335) reflections are shown in Figure 7. Only the uniform layers at the top and bottom of the buffer can be clearly identified. The grading generates a distribution of diffracted intensity between these two features. The residual strain in the starting $InP_{0.94}As_{0.06}$ layer is low enough that we

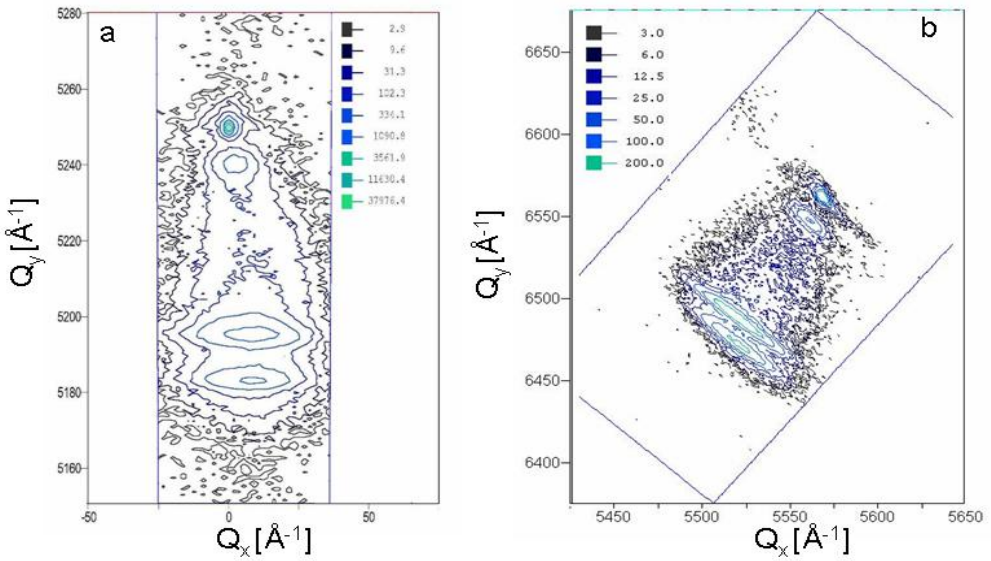


**Figure 10. Reciprocal space maps of a linearly graded InPAs buffer (05-366a) with a 1 µm InGaAs layer on top. a) The (004) symmetric reflection and b) the asymmetric (335) reflection.**

conclude that this layer is completely relaxed. The residual strain and the tilt in the top $InP_{0.64}As_{0.36}$ is comparable to the third layer of 3-step buffers. From the standpoint of HRXRD, the linear graded and 3-step buffers have very similar characteristics.

**Table 7. Summary of structural parameters for 05-366a.**

| InAs Composition [%] | Thickness [Å] | Coherency strain to InP [%] | Tilt [°] | Residual strain X $10^4$ [-] | Relaxation [%] |
|---|---|---|---|---|---|
| 5.6 | 5000 | 0.18 | 0.02 | 0.39 | 97.9 |
| 35.5 | 7000 | 1.15 | 0.10 | 13.4 | 88.1 |

### 2.4.3 Multi-step graded buffer layers

The approach to InPAs buffers NREL has taken is to use thinner layers with smaller composition steps between for each layer. This approach approximates the linear grade used by MIT Lincoln Laboratories. Figure 8 shows the reciprocal space maps

obtained for sample 1-956 taken about the (004) and the (444) reflections. The nine steps used in the structure are clearly identified in both the (004) and the (444) reflections.

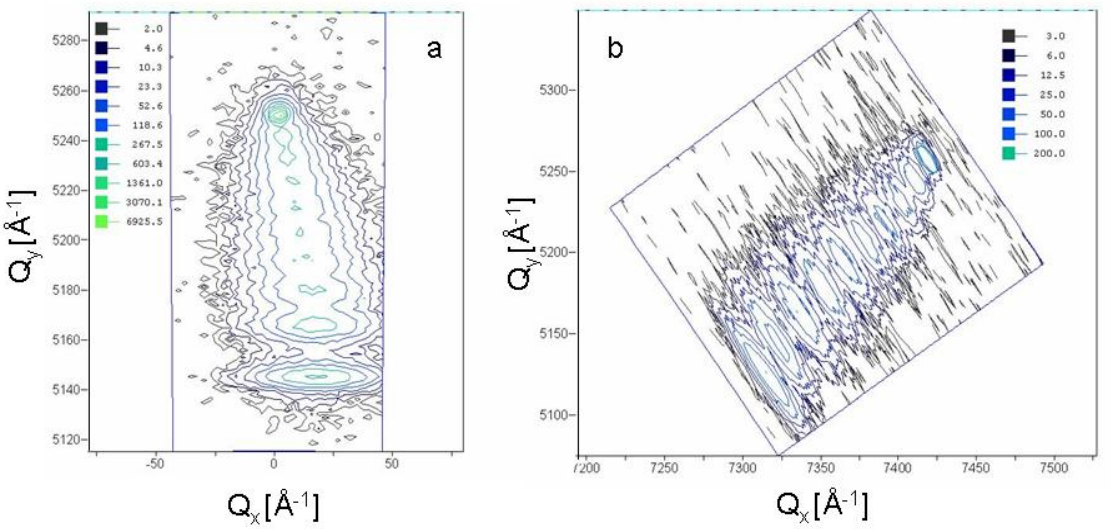


**Figure 11. Reciprocal space maps of a step graded InPAs buffer (1-956) top about the a) (004) and b) (444) reflections.**

**Table 8. Summary of structural parameters for 1-956.**

| InAs Composition [%] | Thickness [Å] | Coherency strain to InP [%] | Tilt [°] | Residual strain X $10^4$ [-] | Relaxation [%] |
|---|---|---|---|---|---|
| 4.5 | 3000 | 0.15 | 0 | 0.05 | 99.7 |
| 9.4 | 3000 | 0.30 | 0.03 | -1.3 | 104.2 |
| 15.7 | 3000 | 0.51 | 0.06 | 0.99 | 98.0 |
| 21.7 | 3000 | 0.71 | 0.06 | 1.06 | 98.5 |
| 28.1 | 3000 | 0.91 | 0.09 | -1.5 | 101.7 |
| 34.1 | 3000 | 1.10 | 0.12 | -0.78 | 100.7 |
| 42.3 | 3000 | 1.37 | 0.18 | -1.05 | 100.8 |
| 50.3 | 3000 | 1.63 | 0.15 | -0.64 | 100.4 |
| 59.2 | 3000 | 1.91 | 0.15 | 10.8 | 97.2 |

Table 8 summarizes the designed and measured parameters for 1-956. The residual strains in the buried and surface layers are comparable to the 3-step and the linearly graded buffer designs. Complete relaxation is observed for all the buried layers. The total thickness of 1-956 is 2.7 µm, comparable to the 2.8 µm for the 3-step and linearly graded buffers, but the coherency strain relieved for 1-956 is 75% larger. This suggests that the 3-step buffer design could be improved by using less material to relieve the same strain.

## 2.5 $In_{0.68}Ga_{0.32}As$ TPV cells on InPAs buffers

The growth of $In_{0.68}Ga_{0.32}As$ on the InPAs buffer layer limits the amount of fundamental information that can be obtained about the underlying buffer layers. For the samples studied the strain state of the first and third buffers and the InGaAs cell could be determined. The strain state of the second buffer could not be determined unambiguously due its overlap with the InGaAs cell. Information from RSMs allow the lattice match between the third InPAs buffer to the InGaAs cell to be measured, critical information to assess the quality of the TPV structure.

Table 9 summarizes some of the parameters for the InGaAs TPV cells measured. Figure 9 shows typical RSMs of the (004) and (335) reflections for a TPV cell. The second buffer cannot be identified due to the large intensity of the InGaAs TPV cell. For this sample the third buffer layer was a shoulder on the InGaAs cell peak as well. The strain and composition of the third buffer peak could be determined using radial linescans of other reflections, such as the (006) and the (444), as discussed in Section 2.2.

**Table 9. Summary of results for the strain relaxed InGaAs TPV cells analyzed.**

| Sample No. (miscut from 100 surface) | InAs Composition $1^{st}/3^{rd}$/cell [%] | Coherency Strain to InP $1^{st}/3^{rd}$/cell [%] | Zn doping level for each layer [$cm^{-3}$] | Residual strain $1^{st}/3^{rd}$/cell X $10^4$ [-] | Relaxation $1^{st}/3^{rd}$/cell [%] |
|---|---|---|---|---|---|
| VE085d | 19.0 | 0.61 | 10 | 3 | 104.9 |
| (2° miscut | 32.9 | 1.05 | 10 | 7 | 93.2 |
| toward [110]) | 69.6 | 0.97 | 1 | 2 | 98.1 |
| VE089d | 17.9 | 0.58 | 10 | 0.7 | 101.5 |
| (2° miscut | 32.3 | 1.03 | 10 | 6 | 94.8 |
| toward [110]) | 67.6 | 0.98 | 1 | 3 | 97.3 |
| VE095d | 17.6 | 0.57 | 10 | -3.0 | 105.3 |
| (2° miscut | 36.5 | 1.18 | 10 | 12.2 | 89.6 |
| toward [110]) | 68.7 | 1.07 | 1 | 4.0 | 96.2 |
| VE152a | 20.2 | 0.65 | 10 | 0.4 | 99.4 |
| (2° miscut | 35.2 | 1.14 | 10 | 15 | 86.3 |
| toward [110]) | 69.7 | 1.04 | 1 | 31 | 68.2 |
| VE161a | 20.2 | 0.65 | 10 | 0.3 | 100.4 |
| (2° miscut | 33.7 | 1.09 | 10 | 4.0 | 96.6 |
| toward [110]) | 69.7 | 0.98 | 1 | 5.7 | 94.1 |
| VE209a | 16.7 | 0.54 | 10 | 2.0 | 103.5 |
| (2° miscut | 27.5 | 0.89 | 10 | 0.8 | 100.8 |
| toward [110]) | 67.9 | 1.02 | 1 | 11 | 43.5 |
| VE235a | 16.5 | 0.53 | 10 | 2.8 | 94.8 |
| (2° miscut | 27.8 | 0.90 | 10 | 4.0 | 95.5 |
| toward [110]) | 67.2 | 0.96 | 1 | 52.7 | 44.9 |

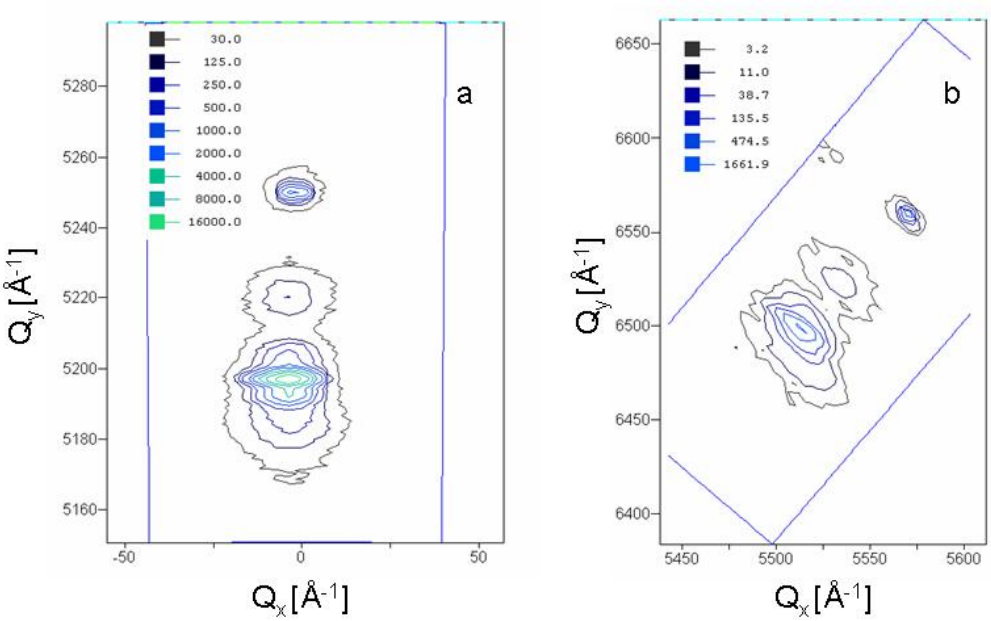


**Figure 12. RSMs of ve089d, an InGaAs TPV cell on a 3-step InPAs buffer, showing a) the (004) reflection and b) the (335) reflection.**

## 2.6 Summary

X-ray based techniques are critical to provide important information about strain and composition of layer in strain-relaxed buffers and TPV devices. The reflections used need to be considered carefully to provide most signal possible as well as the lowest error associated with the residual strain and composition so accurate information is provided for feedback into the crystal growth process.

Three types of samples were considered in this study. Single layers provide a simple structure to look at the effect dopants have on morphology and relaxation. Generally InPAs layers behave like other III-V materials, showing a large regime of metastability and incomplete relaxation over the range of structures considered. Te doped films seem to have more relaxation compared to undoped, Si-, and Zn-doped films. The success of equilibrium models to describe the amount of relaxation and the saturation

of the relaxation is poor leaving a gap in knowledge for the design InPAs buffer structures. 3-step buffers show a much larger amount of strain relief compared to other III-V materials. The lack of residual strain might, in part, contribute to the success of strain-relaxed TPV technology. Other buffer design were evaluated, specifically a linear grade and a uniformly stepped structure. These structures suggest that the 3-step design might not be optimal in terms of achieving a relaxed buffer with the minimum amount of InPAs. InGaAs cells grown on the strain relaxed InPAs buffer obscures some of the buffer features making complete, unambiguous evaluation of the buffer state impossible. Under the best experimental and sample conditions the composition and strain in the InGaAs cell can be determined, the strain state of the top buffer can be evaluated, and the lattice match between the two can be provided. This is sufficient for feedback into the growth process, but limits the scientific investigations that can be done on full TPV device cells.

A preliminary investigation of relaxation of metastable InP0.86As0.14 films was undertaken. The results suggest that critical thickness are a much as a factor of four larger than the Matthew-Blakeslee criteria. A single InPAs buffer was evaluated using x-ray peakwidth techniques to estimate the dislocation densities. The tilt component of the peakwidth gives a screw dislocation density that is an order of magnitude larger than any estimate of the films dislocation density. The twist component of the peakwidth gives a edge dislocation density that fails between the estimates given by XTEM and AFM observations.

# 3 Etch Chemistries for Evaluation of Threading Dislocation Densities

## 3.1 Introduction

The threading dislocations that form at the interface between a relaxed layer and its substrate propagate through the epilayer and end at a surface, either the surface parallel to the surface they were formed in or they make it to an orthogonal surface, represented by the sample edge terminating their propagation. The density of threading dislocations in these films is unknown and could range from 1 x $10^5$ $cm^{-2}$ to over 1 x $10^9$ $cm^{-2}$. Since lower dislocation densities are needed for improvements in the cell performance an effort to rapidly quantify the threading dislocation density in strain relaxed InPAs and InGaAs materials was initiated. The relevant dimensions for the study are established. Since the density of threading dislocations is expected to be high optical microscopy, useful for dislocation in bulk layers was discarded in favor of scanning probe techniques. A survey of the possible chemistries was performed which identified etches that have been used for relevant systems. There are surprisingly few studies on ternary materials to baseline our work. A subset of the identified etch chemistries were experimentally investigated for InPAs and InGaAs. A mixture of HBr:H3PO4, termed the H etch, produce clear pits in InPAs. No acceptable defect etch was found for InGaAs.

## 3.2 Experimental issues associated with etch pit measurements

The proximity of individual threading dislocations sets the resolution required for observing etch pits. Table 10 illustrates the spacing of individual dislocations for different threading densities assuming a random distribution of threads. The average dislocation spacing sets the minimum resolution required by the technique used to observed pits. For low threading dislocation densities between 1 x $10^4$ and 1 x $10^6$ $cm^{-2}$ it should be possible to use optical microscopy to count pits. Optical microscopy is used

heavily in bulk crystal growth research for structural defect evaluation. Higher dislocation densities will not be resolved by optical techniques and higher magnification is needed. Higher magnification can be provided by techniques such as atomic force microscopy (AFM) or secondary electron microscopy (SEM). AFM should be applicable over the range of 1 x $10^7$ to 1 x $10^{10}$ $cm^{-2}$, if probe can be scanned over a sufficiently large window, 50 to 100 µm square, to provide relevant statistics. Thermoionic emission (TE) SEM should have sufficient resolution for the intermediate dislocation densities between 1 x $10^7$ and 1 x $10^8$ $cm^{-2}$. Field emission (FE) SEM should provide resolution at the highest densities of greater than 1 x $10^9$.

**Table 10. Dislocation spacing for increasing threading dislocation spacing assuming a random distribution of threading dislocations i.e. L = $\rho_{td}$.**

| **Threading dislocation density [$cm^{-2}$] x 1 x $10^7$** | .001 | .01 | .1 | 1 | 10 | 100 | 1000 |
|---|---|---|---|---|---|---|---|
| **Average dislocation spacing [µm]** | 100 | 31 | 10 | 3 | 1 | 0.3 | 0.1 |

Etch pit formation requires material to be removed to generated the pit. Most pits formed from threading dislocations take the shape of an inverted pyramid or cone, and can be inclined to the surface. As the tip of the pit gets deeper, the base expands proportionally. This causes closely spaced dislocations to become one pit if the etching is too long or too chemically reactive, which results in a systematic under counting of the dislocations in a film. This increases the demands on the microscopic technique. The average dislocation spacing provided in Table 10 is only an upper end estimate of the resolution required.

In bulk crystal growth samples that are over 0.1 to 1 mm thick are available. The amount of material removed to get a well resolved pits is of only a limited concern since many micrometers can be sacrificed to get clear etch pits. This is not true when dealing

with thin epitaxial films that are only 2 to 3 µm thick. The etch much be sufficiently slow to allow well controlled pits to form or the etch process must be rigorously timed so reproducible defects are produced without sacrificing the entire layer of interest.

### 3.3 Survey of etch chemistries

A significant amount of work has been done on chemical etches that decorate dislocations and other structural defects in InP and GaAs substrate material. This work has been extended to thick (~10 µm) epilayers of lattice matched InGaAsP alloys grown by liquid phase epitaxy on InP. Several etch chemistries were identified that could preferentially decorate dislocations in InPAs and InGaAs. Twelve chemistries were identified and are listed in Table 11. Six of the twelve chemistries were investigated experimentally. Early work on InPAs single layers and buffer identified a 2:1 mixture of $HBr:H_3PO_4$ (H etchant) as a promising chemistry, providing reproducible pit formation on $InP_{0.84}As_{0.16}$. The H etchant along with the other five chemistries investigated targeted $In_{0.68}Ga_{0.32}As$. The H etchant did not appear to be reactive to InGaAs. This is not surprising since the H etchant is only reported to be a defect etchant for InP, suggesting the anion determines etch selectivity. The chromate-based A/B etches proved to be too rapid and uncontrollable, often rapidly removing InGaAs and InPAs layers. Replacing the chromate ion with $HNO_3$, a less reactive oxidizer, in the RC-1 etch did not limit the reaction with the result being similar to the A/B etch. The illuminated $H_3PO_4:H_2O_2$ etchant produces some shallow pits for short times, but completely removes the InGaAs cell in less than 180 seconds. The modified super oxidizer (MSO) composed of 1:1:10 $HF:H_2O_2:H_2O$ removes the cell and most of the third buffer in 30 seconds. The most promising etchant investigated was a diluted Sirtl etchant composed of $HF:CrO_3:H_2O$, using compositions far from those used in the A/B etch.

**Table 11. Identified dislocation selective etchants for InP, GaAs, and InGaAsP.**

| Etch Chemistry | Materials reported | Literature Description | References |
|---|---|---|---|
| HBr:HF (Fujitsu etch) (1) | InP, InGaAsP | Pyramidal pits with orthogonal sides, no pits for HF fraction > 50 | 16, 17, 18 |
| HBr:H3PO4 (H etch) (2) | InP, GaAs, InGaAsP, InPAs | Pit size controlled by H3PO4 content, pits are rounded, some problems with reproducibility | 16, 17, 19, 20, 21 |
| HBr:acetic acid (1:X) (3) | InP | Pits are square pyramids for X < 2, elongate in [110] direction for X >3 | 16 |
| HNO3:H2O:HCl (5) | InP, InGaAsP | Unsuccessful, no clear etch pits | 17, 21 |
| HCl:HNO3:Br2 (RRE) (6) | InP, InPAs, InGaAsP | Forms deep and shallow etch pits | 17, 21, 22 |
| HNO3:HBr (8) | InP | Etchant degrade after mixing, pits are rounded rectangles | 17, 23 |
| Chromate-based etches (A/B etch) (4) | InP, InGaAsP | Forms conical defects on (100) surface | 18, 21, 24, 25, 26, 27, 28, 29, 30, 31, 32, 33, 34 |
| HF:CrO3:H2O(9) (Diluted Sirtl etch) (9) | InP, GaAs | Illumination (laser or white light) required | 35, 36, 37 |
| Molten KOH (7) | InP, GaAs, InGaAs | Experimental problems with use, forms conc. KOH solution | 32 |
| $HF:H_2O_2:H_2O$ (1:1:10) (MSO) | GaAs | Performed under illumination by 500 W tungsten lamp. Forms ridges along [110] | 38 |
| $H_3PO_4$ (85%):$H_2O_2$ (30%) 1:1 | InP, InGaAs | Pre-etched with $H_2SO_4:H_2O_2$ Performed under illumination by 50 W lamp. Forms conical pits. | 39 |
| $HF:HNO_3:H_2O$ with $AgNO_3$ solution (RC-1) | GaAs | Ratios of 1:5-7:8-12 with 1% $AgNO_3$ Others are more specific 2:3:5 with 2.4 x $10^{-3}$ molar $AgNO_3$ solution. | 40, 41 |

## 3.4 InPAs dislocation sensitive etch development

### 3.4.1 Experimental details for InPAs etch development

The general procedure used for InPAs etch evaluations is outlined below:

1) Rinse glassware (2 dishes) with DI $H_2O$. Blow out with $N_2$. Let stand on Khemwipe to dry.
2) Clean samples in acetone, methanol, and isopropyl alcohol. Blow dry with $N_2$.
3) Make up etchant. Use graduated cylinders for all preparation.
4) Prepare beaker of DI water to rinse etched samples.
5) Select a sample, rinse in water, and blow dry. This is the control.
6) Remove a sample, etch in prepared etchant for specified time, rinse with DI water for 60 sec. Blow dry with $N_2$. This step is repeated for all samples in study.
7) AFM the etched area. 10 x 10 µm and 50 x 50 µm scans at 45°.

It was discovered that performing the AFM measurements scanning the probe 45° to the orthogonal cross-hatch pattern improved the quality of images allowing features that would be obscured for orthogonal scanning to be captured in a single scan. Most of the data presented will be taken in such a manner. After the samples were etched, they went directly into a beaker of DI water that was being continuously overflowed with fresh DI water. This limited additional reaction after the sample had been removed from the etchant at the specified time.

### 3.4.2 H etchant (1:2 HBr:H3PO4) with single InPAs layers

This etchant was evaluated using single layers of $InP_{0.86}As_{0.14}$ with a smooth as-grown, morphology. A series of samples were tested for different etching times for the same etchant solution. The atomic force micrograph in Figure 13 shows the surface of the sample treated for 60 seconds in this solution. 60 seconds seemed to produce the sharpest features in this study. The density of the pits is 2.1 x $10^8$ $cm^{-2}$. The pits can be roughly categorized as elongated slits or asymmetric pits, both of which could be generated by the intersection of a threading dislocation with the surface. The other

observation, which can be clearly seen at lower magnification, is that the pits do not nucleate uniformly across the layer, but instead form bands. This would occur if the pits represented individual threading dislocations that were trapped in a bunch by the

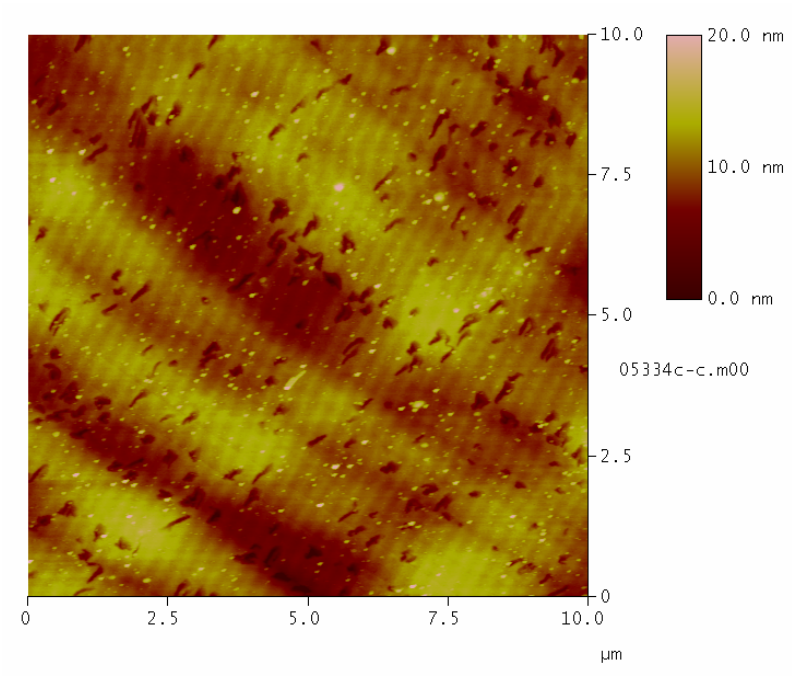


**Figure 13. The surface of 05-334c undoped $InP_{0.82}As_{0.18}$ after treatment with Huber etchant. Major and minor crystal orientations are at 45° to the axis of the image.**

evolving growth topography. The encouraging results for undoped $InP_{0.86}As_{0.14}$ led us to test other InPAs layers that should have a range of threading dislocations densities. Figure 14 shows the surface of InPAs doped with Te. The pit density is slightly lower for this film, 9 x $10^7$ $cm^{-2}$, but is dominated by etching debris on the surface. If the pits represent threading dislocations, this supports the proposal that Te doping improves the buffer, potentially by increasing the dislocation velocity and allowing fewer dislocations to get the same amount of relaxation. Literature results on undoped and heavily n-type (n ~ 8E18 $cm^{-3}$) InP doped with sulfur showed a large asymmetry in the velocities for α and β dislocations.[42] For undoped InP, β dislocations have higher propagation velocities

approaching 1 x $10^{-4}$ cm/second, while α dislocations have lower propagation velocities of 1 x $10^{-5}$ cm/second. For sulfur doped InP this situation is reversed, the α dislocations have higher propagation velocities of 1 x $10^{-4}$ cm/second and the β dislocations have lower velocities of 1 x $10^{-6}$ cm/second. This enhancement of dislocation propagation my also exist for InPAs layers.

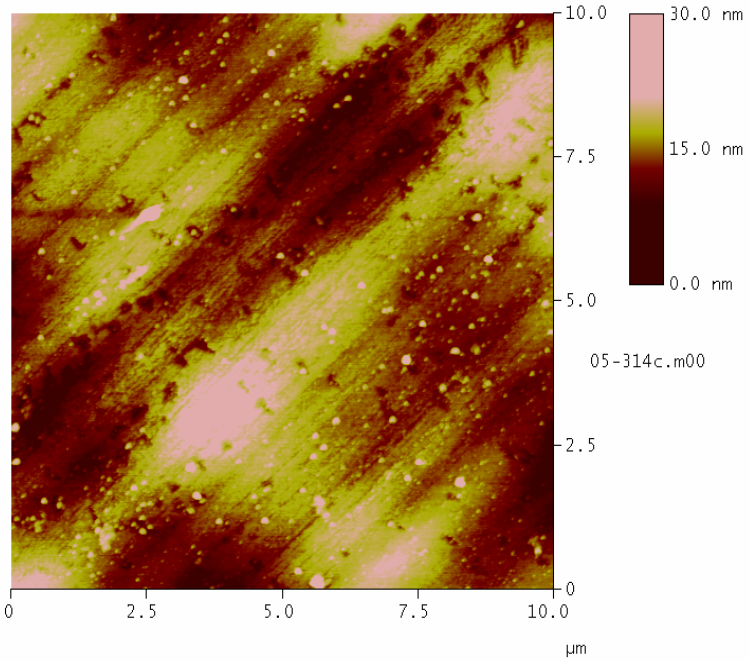


**Figure 14. The surface of 05-331c Te: $InP_{0.82}As_{0.18}$ after treatment with Huber etchant Major and minor crystal orientations are at 45° to the axis of the image.**

Higher pit densities were observed for undoped InPAs with an InAs composition of 32.6 %. A representative image is shown in Figure 15. The pit density is 3.9E8 $cm^{-2}$, approximately two times larger than for an undoped sample with an InAs composition of 18.0%. This is consistent with the belief that the density of dislocations is proportional to the initial coherency strain and supports the belief that grading, either in a stepwise or continuous manner limits dislocation formation and reduces the need for later removal or annihilation.

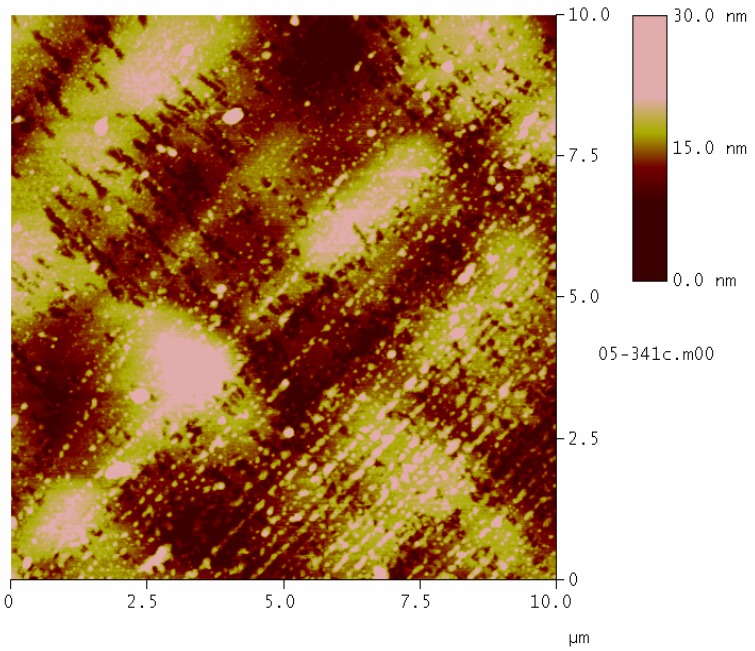


**Figure 15. The surface of 05-341c undoped $InP_{0.68}As_{0.32}$ after treatment with Huber etchant Major and minor crystal orientations are at 45° to the axis of the image.**

### 3.4.3 H etchant (1:2 HBr:H3PO4) with InPAs buffers

Limited investigation of InPAs 3-step buffers with the H etchant was done during the study. InPAs buffers have significant cross-hatch morphology, characteristic of thick, heavily strain relaxed layers. This morphology is shown in Figure 16a, for the as-received Zn:InPAs buffer. The density of small pits was over 1.1 x $10^8$ $cm^{-2}$. When the sample is etched, the roughness is amplified. Small pits become deeper and expand laterally across the surface. Clear identification of new features cannot be performed in a quantitative manner. This is shown in Figure 16b, where the large pits on the right side of the figure have replaced the smaller pits that are observed in the as-received sample. Some of the issue with this study is that Zn-doping causes problems with the morphology. A possible solution would be to study n-type InPAs material.

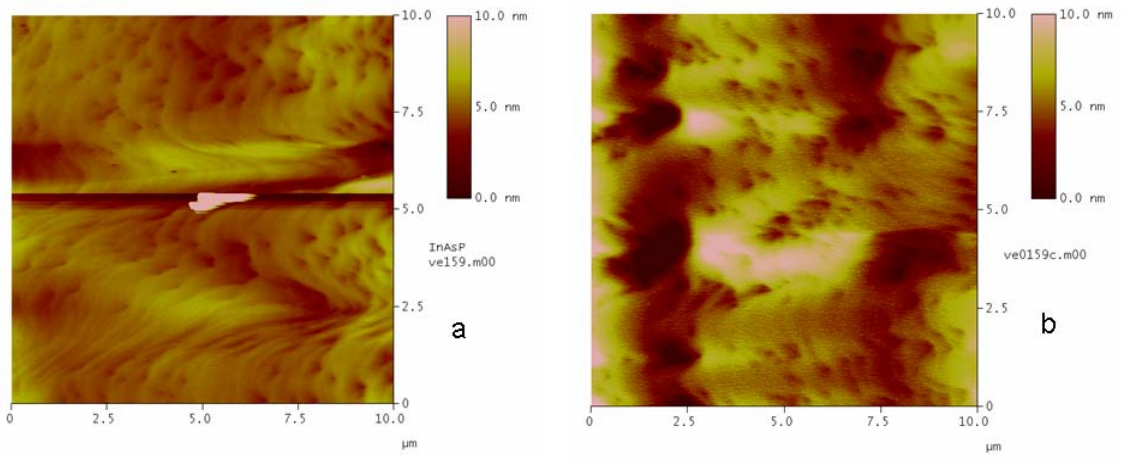


**Figure 16. AFM images showing the a) as-received Zn:InPAs 3-step buffer and b) the etch buffer using the H etchant for 60 sec.**

## 3.5 InGaAs dislocation sensitive etch development

### 3.5.1 Experimental details for InGaAs etch development

The procedure for the InGaAs etch evaluations was complicated by the fact that TPV015 cells were used for evaluation. The InGaAs layers were prepared by chemically removing the InGaAs contact and InPAs window layers from a standard TPV cell, which is shown in Table 12 below.

**Table 12. Description of TPV015 structure used for InGaAs etching studies. InGaAs contact and InPAs window layers were removed to look only at the InGaAs emitter layer.**

| Layer Description | Thickness [µm] | Material | Dopant | Doping level [$cm^{-3}$] |
|---|---|---|---|---|
| Contact | 0.05 | $In_{0.68}Ga_{0.32}As$ | Si (n-type) | 1.00E+19 |
| Window | 0.05 | $InP_{0.66}As_{0.34}$ | Si (n-type) | 2.00E+18 |
| Emitter | 0.30 | $In_{0.68}Ga_{0.32}As$ | Si (n-type) | 5.00E+18 |
| Base | 2.50 | $In_{0.68}Ga_{0.32}As$ | Zn (p-type) | 1.00E+17 |
| Back Surface Field | 0.05 | $InP_{0.66}As_{0.34}$ | Zn (p-type) | 2.00E+18 |
| Tunnel Junction | 0.05 | $In_{0.68}Ga_{0.32}As$ | Zn (p-type) | 1.00E+19 |
| Tunnel Junction | 0.05 | $In_{0.68}Ga_{0.32}As$ | Si (n-type) | 1.00E+19 |
| Graded Buffer | 1.40 | $InP_{0.66}As_{0.34}$ | Si (n-type) | 1.00E+19 |
| | 0.70 | $InP_{0.74}As_{0.26}$ | Si (n-type) | 1.00E+19 |
| | 0.70 | $InP_{0.84}As_{0.16}$ | Si (n-type) | 1.00E+19 |
| InP Nucleation Layer | 0.20 | InP | NID (n-type) | 1.00E+15 |
| Semi-insulating substrate | | InP | Fe | Semi-insulating |

The general procedure followed for InGaAs layer preparation and etching is outlined below:

1) Rinse glassware (2 dishes) with DI $H_2O$. Blow out with $N_2$. Let stand on Khemwipe to dry.
2) Clean samples in acetone, methanol, and isopropyl alcohol. Blow dry with $N_2$.
3) Prepare 1:1:18 $H_2SO_4$:$H_2O_2$:$H_2O$ (Caro's etchant) as first etchant in a cleaned glass container. Use 10 mL $H_2SO_4$, 10 ml $H_2O_2$, and 180 mL DI $H_2O$. Use graduated cylinders for all preparation.
4) Pour up concentrated HCl in a cleaned glass container. Use enough to cover sample in dish.
5) Prepare etchant.
6) Prepare two (2) beakers of DI water to rinse etched samples.
7) Etch each sample for 32 seconds in Caro's etchant. Use a basket to hold all samples.
8) Etch each sample for 80 seconds in concentrated HCl. Use a basket to hold all samples.
9) Rinse samples in DI water. Leave in DI water and remove while performing individual experiments.
10) Remove a sample and blow dry. This is the control.
11) Remove a sample. Etch for specified time. Rinse with DI water for 60 sec. Blow dry with $N_2$. This step is repeated for all samples in study.
12) AFM the etched area. 10 x 10 µm and 50 x 50 µm scans at **45°**.

Caro's etchant, 1:1:18 $H_2SO_4$:$H_2O_2$:$H_2O$, was identified and verified as a selective etchant for InGaAs to $InP_{1-y}As_y$ with y less than 0.4.[43] The Caro's etchant was used to remove the InGaAs contact layer of the structure. The 50 nm InGaAs layer could be remove in 16 seconds, so 100% overetch was used to insure this layer cleared. The removal of the InPAs window layer was not as simple since no selective etchants could be found for InPAs over InGaAs. HCl (32% by volume) will etch InP and InAs, but not GaAs so this was selected as the etchant to remove InPAs from InGaAs.[44] A timed etch was investigated to remove the InPAs window completely, but leave as much of the InGaAs cell as possible. 20 seconds did not clear the InPAs window completely, but 40 seconds cleared most of the window. A 100% overetch was used in the recipe. During the removal of the InGaAs contact and InPAs window layers care was taken not to increase the roughness of the surface or introduce surface topography that might be misidentified as being due to dislocation decoration. Figure 16 shows the morphologies for the as-received (Figure 17a) and the chemically decapped cells (Figure 17b). Significant new topography is generated during the etching process. The large scale cross hatch pattern still remains, but the finer features are modified. The diagonal mounds observed in the as-received surface give way to cigar-shaped pits that are repeated across the etched surface. The density of pits is about $4.7 \times 10^7$ $cm^{-2}$. The RMS roughness of the two surfaces is very similar; 10.7 nm for the as received and 8.3 nm for the etched surface. The features identified could easily be interpreted as dislocation-related pits, however **{Need help here!!!!!?????}**

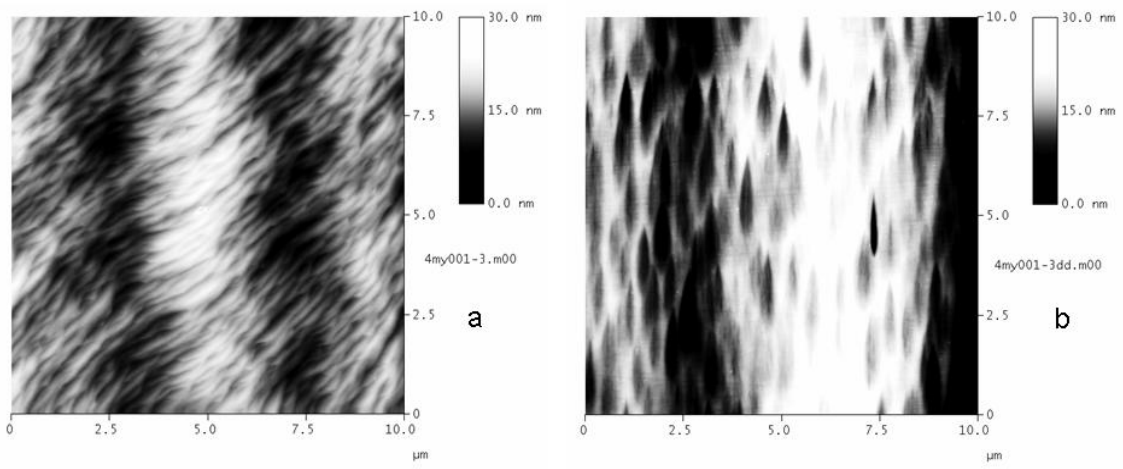


**Figure 17. AFM images of 4my001-3 a) before chemical treatment and b) after removal of removal of InGaAs contact and InPAs window layers.**

Some of etchant investigated required illumination by above bandgap light to in initiate the etching process. Illumination was provided by a 120 W 24 V lamp mounted to an elliptical reflector mounted on optical rails as shown in Figure 18. The sample was place at the approximate focal point of the reflector. The power density produced was 0.2 W/cm$^2$. A manually variable inductor was used to limit the power on the bulb to 20 V.

**Figure 18. Lamp and experimental equipment used for providing illumination to samples.**

### 3.5.2 H etchant (1:2 HBr:H3PO4) with InGaAs

The Huber etchant was also tested with $In_{0.68}Ga_{0.32}As$ n-type emitter layer of TPV015 structures. The H etchant did not introduce any new features in the AFM images, it only magnified and sharpened the cell-boundary morphology observed in Figure 17b. This suggests that the H etchant is not useful in decorating dislocations for InGaAs. The lack of modification to the InGaAs surface is in agreement with the literature that indicates that the H etchant has only been used for InP investigations and is not relevant for As-containing materials.

### 3.5.3 AB etchants ($HF:CrO_3:H_2O$) with InGaAs

The lack of unambiguous pitting on InGaAs layers with the Huber etchant dictated that other etch chemistries should be investigated. A general class of defect sensitive etchants are Sirtl etchants, which use $CrO_3$ as the oxidant and HF as the acidic component to dissolve the oxidized semiconductor into solution. The AB etchant is a subclass and has been used successfully for identification of treading dislocations in

GaAs substrates. It consists of 0.3 gms $AgNO_3$ in 40 mL of DI $H_2O$ and 40 mL HF to form part A which is combined with part B consisting of 40 gms of $CrO_3$ in 40 mL of DI $H_2O$ prior to use. $AgNO_3$ is believed to moderate the etchant and limit the reaction rate, however, the results obtained in our study suggest that the etching rate is still very high for InGaAs. Figure 19 below is the surface produced after 60 seconds in an AB etchant. The pit density is $2.4 \times 10^8$ $cm^{-2}$. The cigar shaped ellipses are still present on the surface, but they are much deeper and pits with a round perimeter have formed, similar to what was observed for InPAs with the Huber etchant. The troubling observation is that the pits formed after 60 seconds disappear upon extending the etching time to 180 seconds. Literature results suggest that InGaAs films can be removed from GaAs by the AB etchant very rapidly.[45,46] This is shown to be the case for $In_{0.68}Ga_{0.32}As$ on InPAs by the HRXRD linescans shown in Figure 20. Sample A, the control, shows four clear peaks dominated by the substrate and the InGaAs peak. The intensity of the InGaAs peak is reduced for sample C, 60 second exposure; and it is completely removed for the for sample D, 180 second exposure. This shows that the AB etchant used for GaAs substrates is too aggressive to use for InGaAs layers.

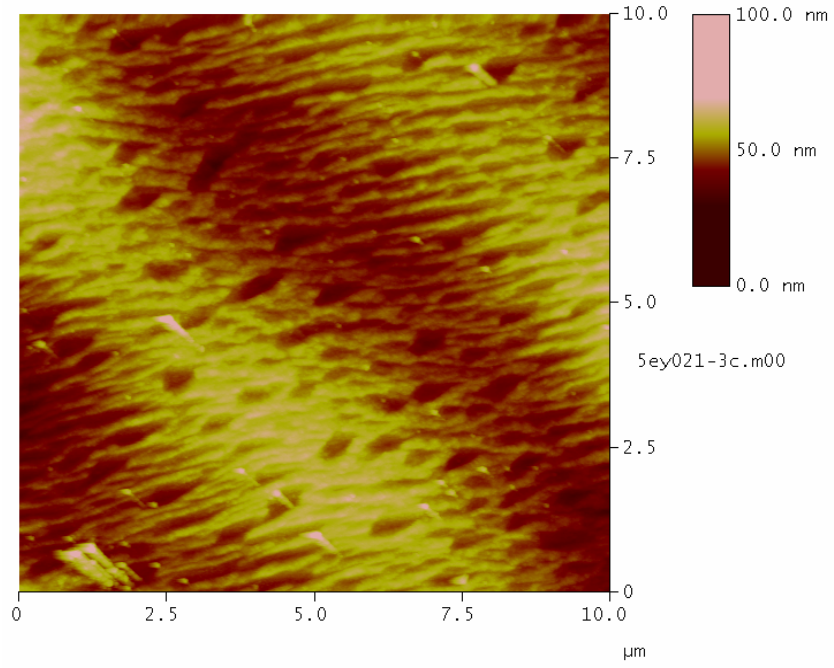


**Figure 19. The surface of 5ey021-3 after chemical treatment to remove the top layers and expose the InGaAs emitter and 60 seconds in the AB etchant. Major and minor crystal orientations are at 45° to the axis of the image.**

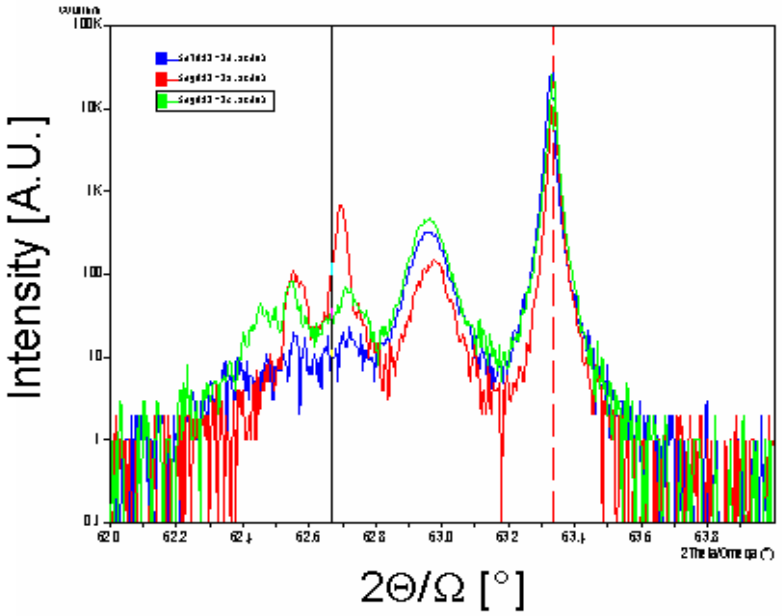


**Figure 20. HRXRD about the (004) reflection for the control sample (sample A - red) and samples etched for 60 seconds (sample C – green) and 180 seconds (sample D - blue). No InGaAs cell is left after 180 seconds in the etchant.**

Previous work on InGaAs on GaAs suggested that diluting the AB etchant with excess HF would slow the etch rate and allow it to retain its defect sensitive characteristics. A 1:3 solution of AB etchant to HF was tried. Figure 21 below shows the surface after only 30 seconds of etching. The surface is similar to that obtained for the AB etchant after 60 seconds, suggesting that the reaction is speeding up. This is believed to be the case since for 60 seconds or longer the surface is dominated by growth morphology and no longer has any pits that are clearly visible.

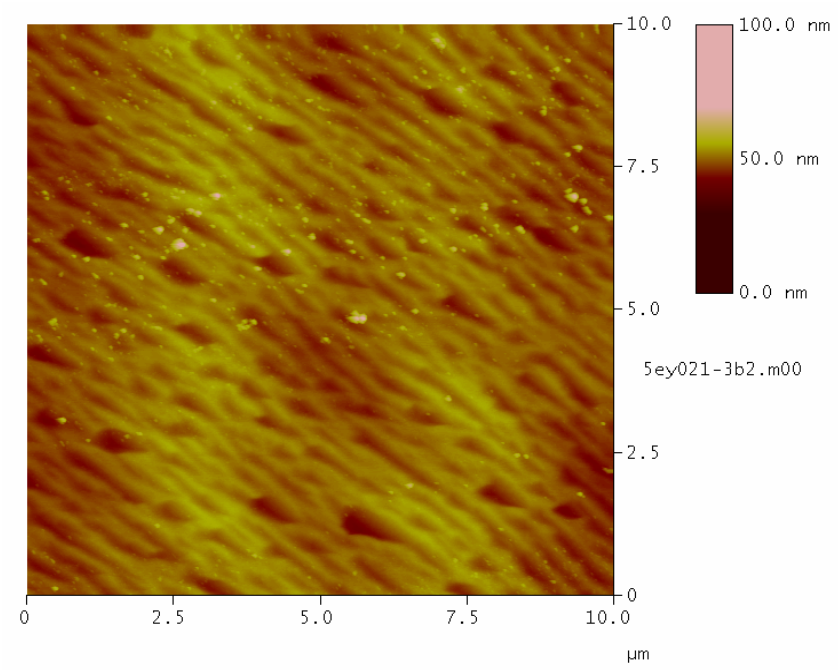


**Figure 21. The surface of 5ey021-3 after chemical treatment to remove the top layers and expose the InGaAs emitter and 30 seconds in the 1:3 AB etchant:HF. Major and minor crystal orientations are at 45° to the axis of the image.**

### 3.5.4 RC-1 ($HF:HNO_3:H_2O$) with InGaAs

Another technique to reduce the reaction between the film and the solution is to use a weaker oxidizer than $CrO_3$. For GaAs this has already been investigated and is termed the RC-1 etchant.[40,41] 20 mL of HF and 30 mL $HNO_3$ were added to 25 mL of DI $H_2O$, producing a 4:6:5 ratio. $AgNO_3$ solution was prepared by mixing 0.816 grams of $AgNO_3$ with 500 mL of DI water in a volumetric flask. 25 mL of the $AgNO_3$ solution

was added to the acid mixture to make a 2:3:5 ratio of acid to water. Figure 22 shows the film surface after the control sample and a sample that was etched for 30 seconds in RC-1 solution. The control (Figure 22a) has the same general morphology observed in TPV015 cells that have had the contact and window layers removed. The background of for the 30 second etch sample (Figure 22b) is closer to the as received morphology. The pits are 1 to 10 µm across and over 100 nm deep, suggesting a very rapid reaction with the film.

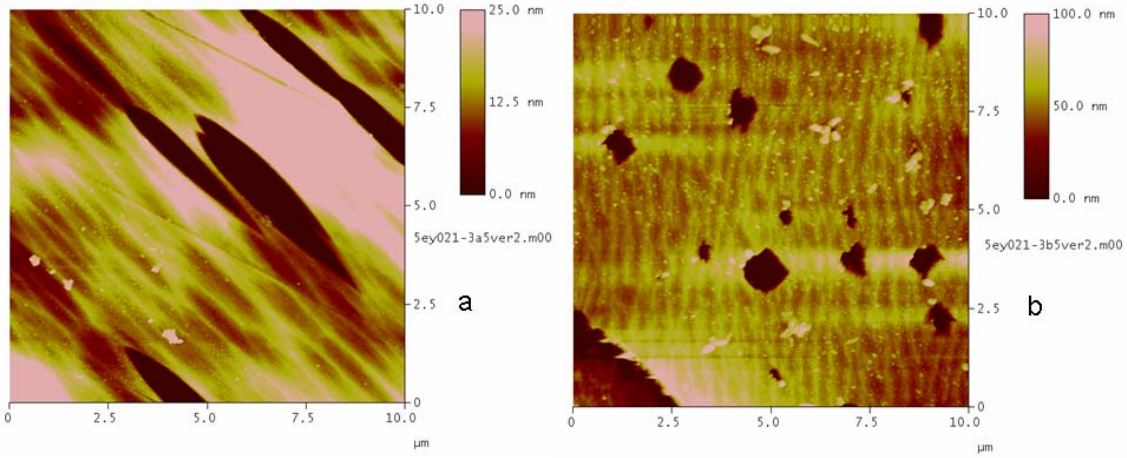


**Figure 22. AFM image of the control and a 30 second RC-1 etch. The regular cigar shaped pits are replaced by large pyramidal pits. Major and minor crystal orientations are at 45° to the axis of the image.**

The features obtained in only 30 seconds of etching suggest that the InGaAs film has been removed. Using TCXRD of the control and etch samples we can see in Figure 23 that this is indeed the case. None of the cell or the top two buffers remains after even this short etch time short etch time.

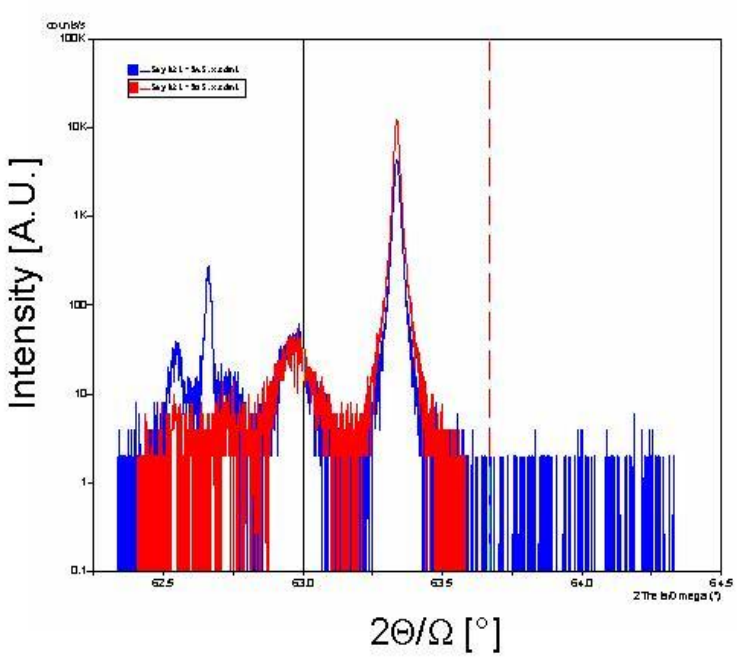


**Figure 23. TCXRD taken around (004) showing the control sample (blue curve) and the sample etched for 30 seconds in the RC-1 etchant (red curve). Most of the layers have been removed in a during the etch, leaving only the first buffer layer.**

### 3.5.5 Illuminated etchants

Some defect sensitive etchants are controlled by the electrochemical generation of holes in the semiconductor by above bandgap illumination. These etchants have the potential for a high degree of control that is not possible with the previously investigated solutions that are controlled by the amount of time the etchant is in contact with the sample surface.

#### 3.5.5.1 $H_3PO_4$(85%):$H_2O_2$(30%)

$H_3PO_4$(85%):$H_2O_2$(30%) in a ratio of 1 to 1 has been used for defect decoration on thick layers of InP and lattice matched InGaAs.[39] Etching for 30 seconds produced the pitted surface shown in Figure 24. The pit shape and depth are similar to what was observed for the variations of the AB etchant that were investigated. The pits persist for short etching times, but for etch times of 180 seconds or longer individual pits are not clear and lower magnification is dominated by orthogonal cross-hatching. The transition

to different morphologies suggests that the InGaAs layer may have been removed, however, evaluation of this using XRD as for the AB etchant was not performed to prove this speculation.

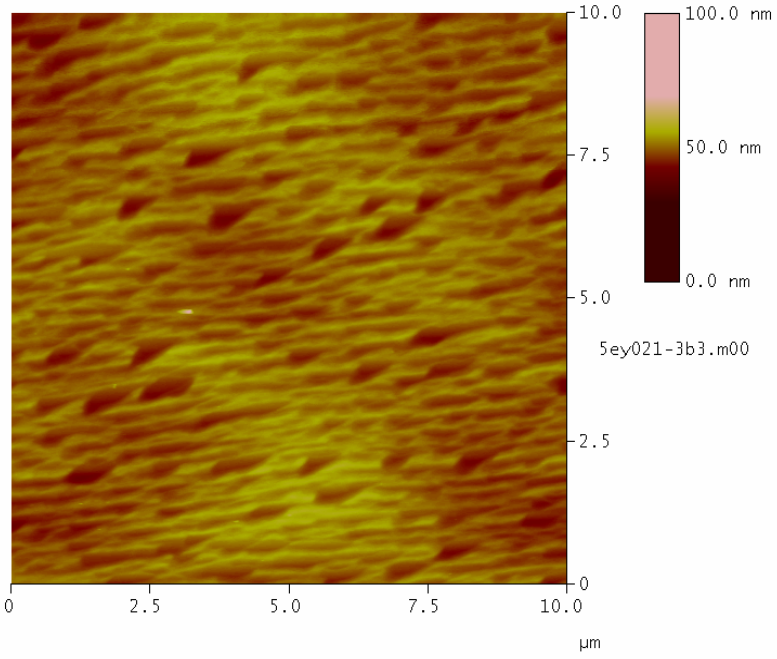


**Figure 24. The surface of 5ey021-3 after chemical treatment to remove the top layers and expose the InGaAs emitter and 30 seconds in the 1:1 $H_3PO_4$(85%):$H_2O_2$(30%). Major and minor crystal orientations are at 45° to the axis of the image.**

### 3.5.5.2 Modified super oxidizer

Modified super oxidizer (MSO) is another illuminated etchant that was investigated. It consists of HF(48%), $H_2O_2$ (30%), and DI $H_2O$ in a 1:1:10 ratio.[38] Illumination was provided using the same lamp described for the $H_3PO_4$:$H_2O_2$ etchant study. The MSO etchant is not completely controlled by direct illumination, suggesting it either has limited reactivity in the dark or is activated by small amounts of room light. Figure 25 shows the surface obtained for a 30 second exposure to MSO without intentional illumination. The first defects that form appear to be expansions of the cigar-shaped ellipses that were observed previously after stripping off the contact and window layers

to expose the underlying InGaAs emitter layer. These defects expand upon illumination and persist on the surface up to 60 seconds. The preferential orientation of the ellipses, without orthogonal features, casts significant doubt that they are related to dislocations.

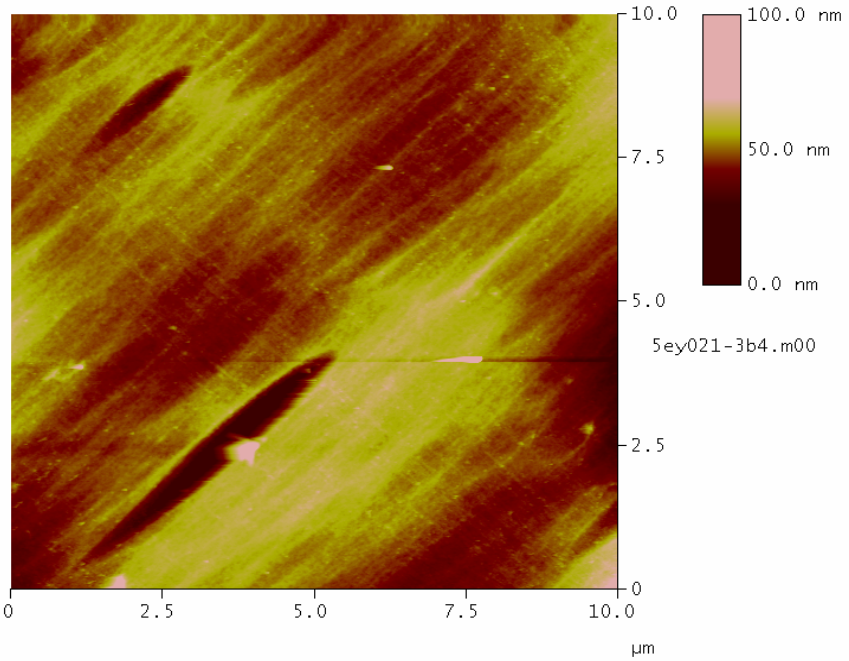


**Figure 25. The surface of 5ey021-3 after chemical treatment to remove the top layers and expose the InGaAs emitter and 30 seconds without illumination in the 1:1:10 HF(48%):$H_2O_2$ (30%):DI $H_2O$ MSO solution. Major and minor crystal orientations are at 45° to the axis of the image.**

At 180 seconds the ellipses have vanished and the morphology returns to what has been observed previously for the AB and $H_3PO_4$:$H_2O_2$ mixtures. An example is given in Figure 26. The pits form along ridges that were not visible at earlier stages of the etching.

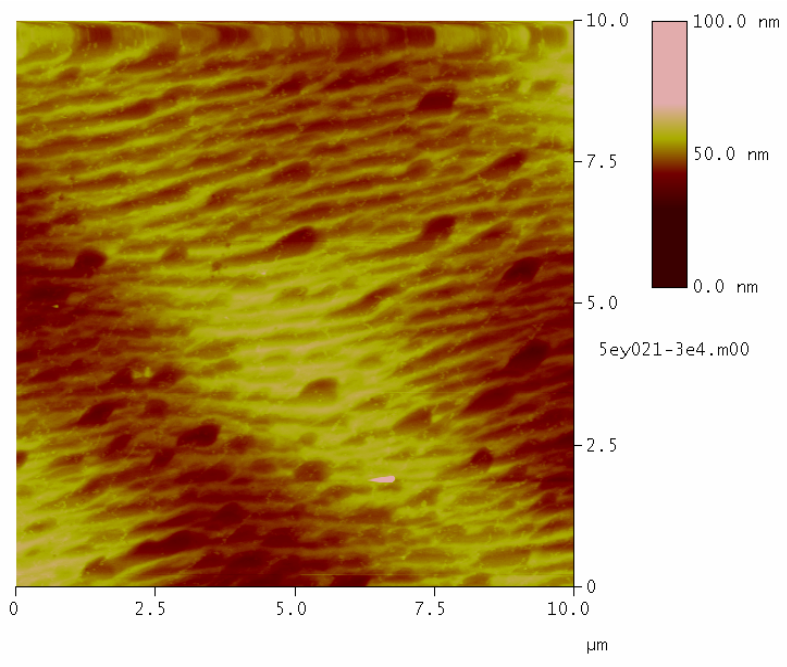


**Figure 26. The surface of 5ey021-3 after chemical treatment to remove the top layers and expose the InGaAs emitter and 180 seconds with illumination in the 1:1:10 HF(48%):$H_2O_2$ (30%):DI $H_2O$ MSO etchant. Major and minor crystal orientations are at 45° to the axis of the image.**

### 3.5.5.3 Sirtl-based etchants

Weyhers, et al. have performed an exhaustive evaluation of the general class of Sirtl etchants, combinations of $CrO_3$, HF, and $H_2O$, mapping out the effect of composition on the sensitivity of the etchant to defects for GaAs.[35,36,37] Their evaluation suggested that if specific volume compositions of this mixture, when used as an illuminated etchant, could provide the desired sensitivity necessary to observe structural defects in epilayers. The type of feature formed by Sirtl etchants is not a pit, but a hillock that projects out of the surface. This represents a challenge for AFM because debris from the etching process can be easily confused with hillocks. This study utilized the observation from the AB etchant study that long etch times do not produce improved defect sensitivity because the planar surface is reacting and the ability to resolve features degrades rapidly. Our studies concentrated on a single etch time, 60

seconds and used the composition of the etchant with deionized $H_2O$ as the varied parameter. Figure 14 shows an InGaAs surface exposed to a 1 to 1 mixture of HF(48%) and a 33 weight percent solution of $CrO_3$ in water. It is impossible to tell the origin of the collections of hillocks that seems to form in the valley of the cross hatch pattern. It could be groupings of threading dislocations known as pile-ups, but it is more likely due to etching debris that has collected on the surface of the wafer. Further analysis might be done with a field emission SEM to see if any contrast that could distinguish between different structures on the

surface.

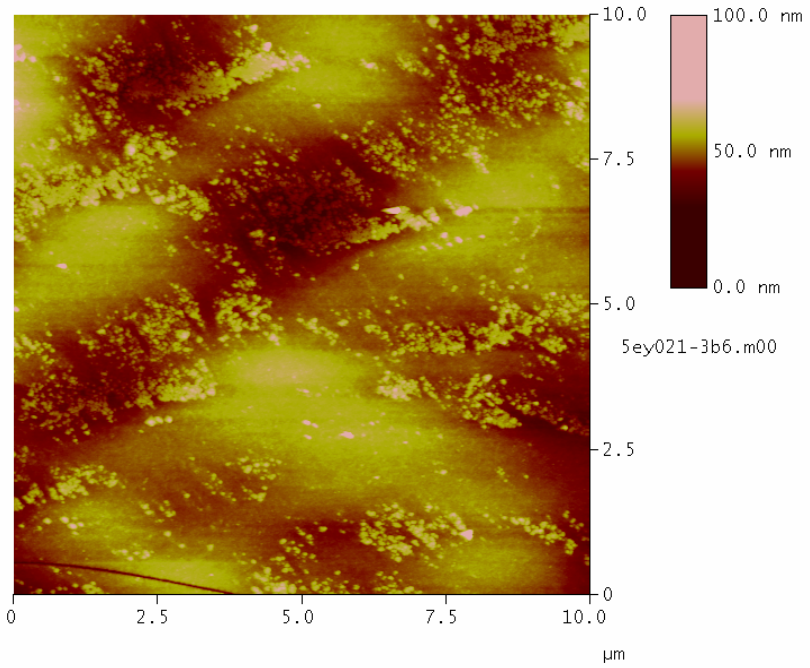


**Figure 27. The surface of 5ey021-3 after chemical treatment to remove the top layers and expose the InGaAs emitter and 60 seconds with illumination in the 1:1 HF(48%):$CrO_3$ (33 wt%) Sirtl etchant. Major and minor crystal orientations are at 45° to the axis of the image.**

Further dilution of the Sirtl etchant with deionized water starts to recover some of the features that have been previously observed for etched InGaAs layers. Figure 15 shows an InGaAs surface that has been etched for 60 seconds in 1 to 1 HF and $CrO_3$

solution that has been diluted with 4 parts of deionized water. The cigar-shaped depressions that are associated with the uncapped InGaAs emitter layer are present.. Significant amounts of etching debris/hillocks are also present. The appearance of the elliptical depressions suggests that the etchant needs longer to decorate any structural defects.

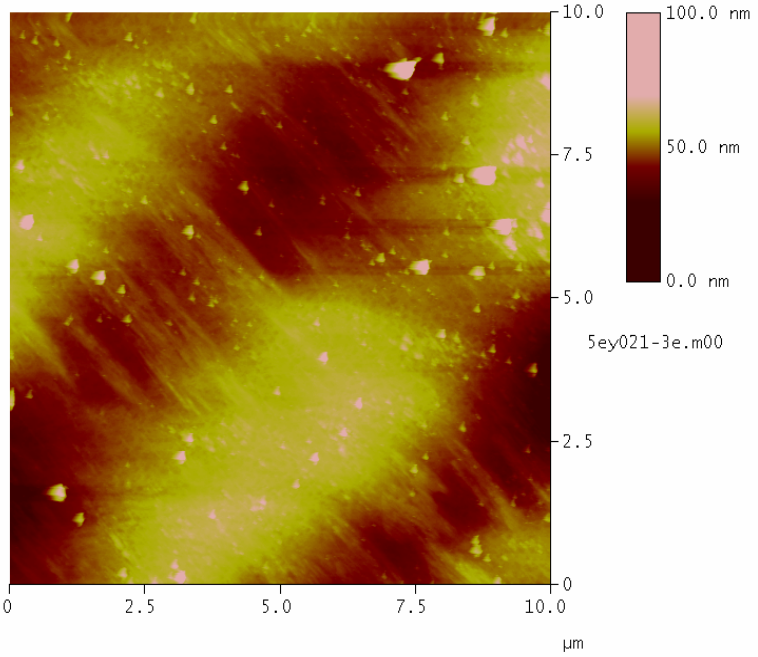


**Figure 28. The surface of 5ey021-3 after chemical treatment to remove the top layers and expose the InGaAs emitter and 60 seconds with illumination in the 1:1 HF(48%):$CrO_3$ (33 wt%) Sirtl etchant diluted with 4 parts of deionized water. Major and minor crystal orientations are at 45° to the axis of the image.**

## 3.6 Summary

Several general observations were made during the testing of the defect sensitive etchants. The features produced for the times investigated were not visible using optical, phase contrast (Nomarski) microscopy. Thermoionic emission SEM does not have sufficient resolution to image the features generated on the surface. Atomic force microscopy has the right resolution, but it also has some limitations. If the decoration results in positive defects, such as hillocks, other information about the defects must be

used to confidently distinguish them from debris from the etching process. A field emission SEM may provide the combination of resolution and qualitative chemical sensitivity that might identify the features associated with structural defects.

The features seemed to have the best resolution at low etch times, between 30 and 60 seconds. Longer etch times seemed to form features that were considered the combination of smaller defects or resulted in removal of the layer. This leads to the question, what is the optimum etching time to limit aliasing of features and provide maximum resolution? This was not directly answered in these studies, but shorter times are superior to long etch times. This is due to the density of features identified as potentially associated with threading dislocations. None of the studies performed had surface feature densities below $1 \times 10^6$ $cm^{-2}$ and most of the features densities exceeded $1 \times 10^8$ $cm^{-2}$. The correlation of these counts to actual threading dislocation densities was not made in these studies.

# 4 Transmission Electron Microscopy of strain relaxed buffers and TPV devices

## 4.1 Cross-sectional transmission electron microscopy (XTEM)

Two XTEM studies were conducted at Sandia. The first was an analysis of the effect of chemical treatment on the interface between InGaAs TPV cell and SiN dielectric used in monolithic interconnected module (MIM) processing. The samples were provided from Bettis Atomic Power Laboratory. The second attempted to look at dislocation propagation in a 3-step buffer grown at MIT Lincoln Laboratory.

## 4.2 InGaAs/SiN interfacial analysis.

The chemical treatment of processed TPV cells prior to SiN dielectric deposition can enhance or degrade TPV cell performance. Three chemical treatments, which are listed in Table 13, were considered in this study. The samples considered were not TPV cells, but structures that mimic the structural properties of TPV cells consisting of 3.3 µm of p-InGaAs on a 2.9 µm n-InPAs graded buffer.

**Table 13. Chemical treatments considered in the study of SiN/InGaAs interface formation and stoichiometry.**

| Sample Number | Passivation treatment prior to SiN deposition |
|---|---|
| NREL 1-1006 Q1 | None |
| NREL 1-1006 Q2 | $HCl:H_2O$ |
| NREL 1-1006 Q4 | $NH_4OH:H_2O$ |

The samples were manually cleaved from the quarter wafer provided and thinned to electron transparency using a focused ion beam (FIB). AuPd alloys was deposited on the SiN to eliminate sample charging during the FIB process. Figure 29 below shows a representative image from Sample NREL 1-1006 Q1, which shows the SiN on top of the InGaAs layer. The InPAs buffer is out of the field of view, below the InGaAs layer. The square box in the center was characterized by sampling the x-rays emitted from the volume that are excited by the electron beam. The x-rays generated are characteristic of

the materials present. The spectra emitted from the center box and the control areas in the InGaAs and SiN are shown in Figure 30 below. By isolating the interface only, as done in Figure 31 for NREL 1-1006 Q1, the primary components are of this layer are silicon and oxygen with varying amounts of gallium, indium, and arsenic. Oxygen is of concern, since it represents an extrinsic species, as well as the relative amounts of gallium, indium, and arsenic, since these represent decomposition products from the reactive deposition of SiN on the InGaAs. Figure 32 shows the same interface spectrum, for NREL 1-1006 Q2. The relative amount of oxygen, gallium, indium, and arsenic are all lower for this treatment. Figure 33 shows the same analysis for NREL 1-1006 Q4. For this sample the interfacial oxygen is similar to that for NREL 1-1006 Q2, but the indium, gallium, and arsenic present has risen to levels above that found in the control sample, NREL 1-1006 Q1. This suggests that the $HCl:H_2O$ is less reactive and also removes some of the oxide formed on the InGaAs surface during prior processing. None of the treatments were able to completely remove oxygen from the interface.

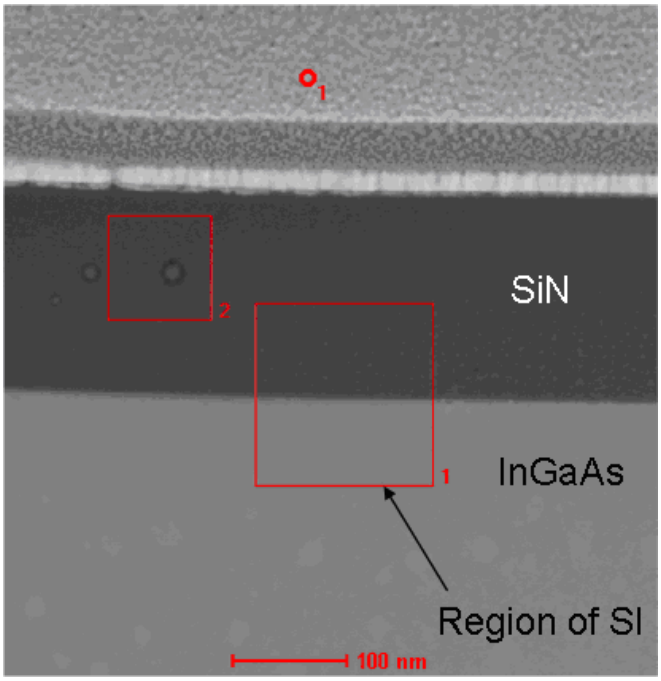


**Figure 29. XTEM image of the interface between InGaAs and SiN. Region 1 was used to get information about the interface between these two layers. Region 2 was a control to get the SiN spectrum. Region 3 (not visible in this image) was used to get the InGaAs signal.**

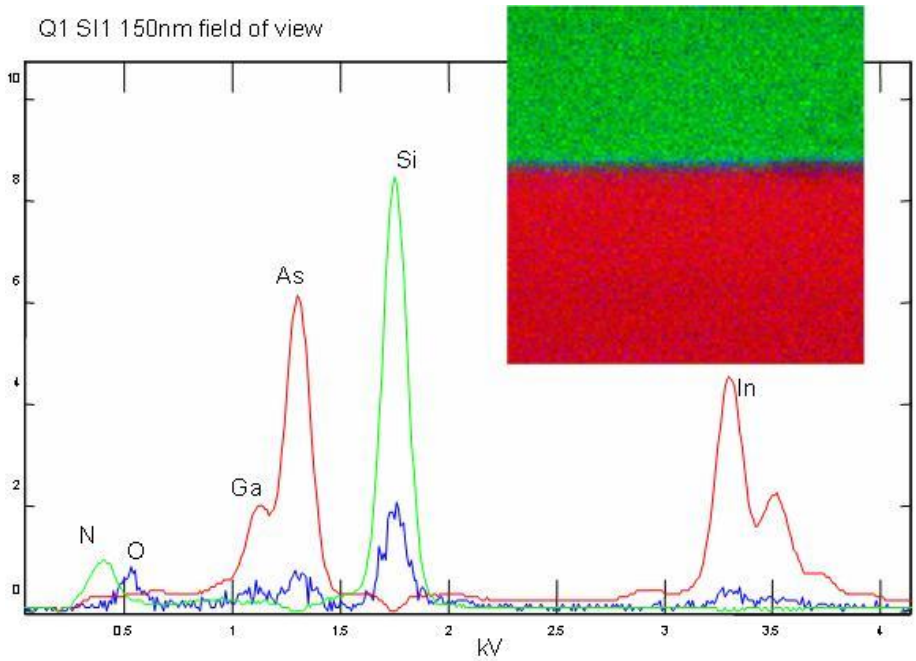


**Figure 30. X-ray spectrum from different areas of NREL 1-1006 Q1. The red spectrum corresponds to the InGaAs layer, the green spectrum from the SiN layer, and the blue spectrum is the interface between the two.**

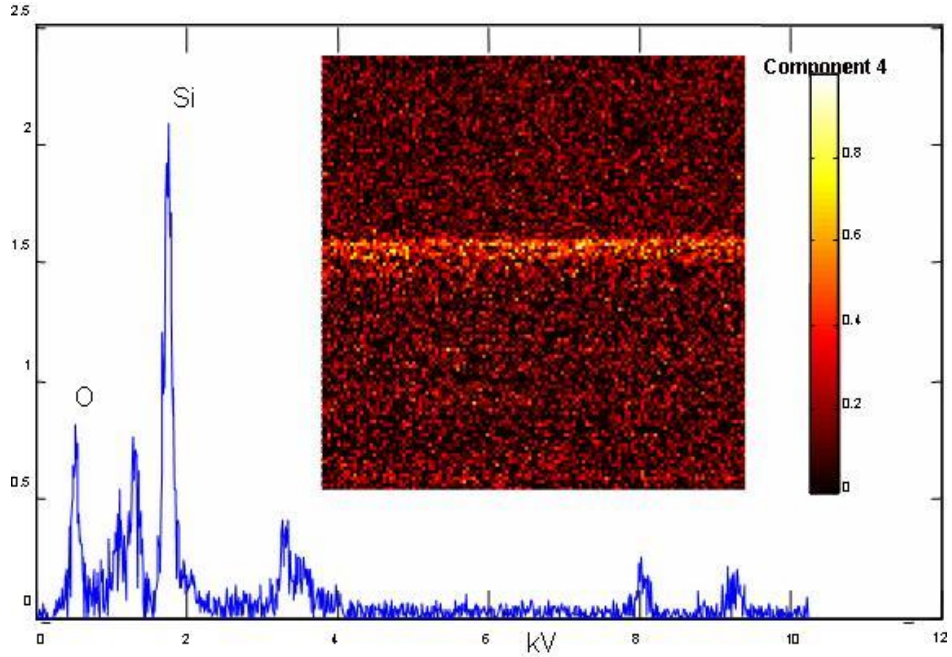


**Figure 31. X-ray spectrum from the interface layer for NREL 1-1006 Q1**

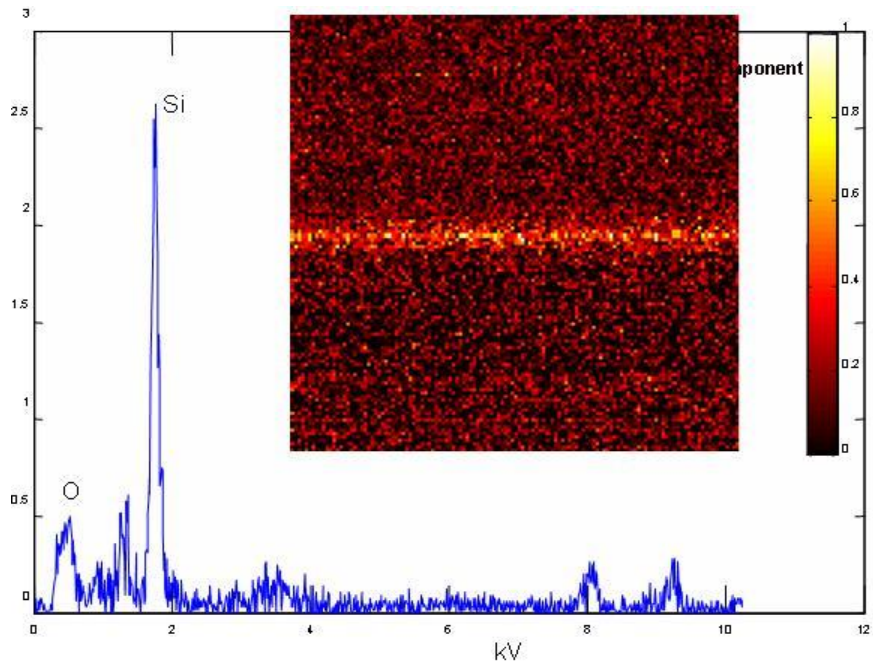


**Figure 32. X-ray spectrum from the interface layer for NREL 1-1006 Q2**

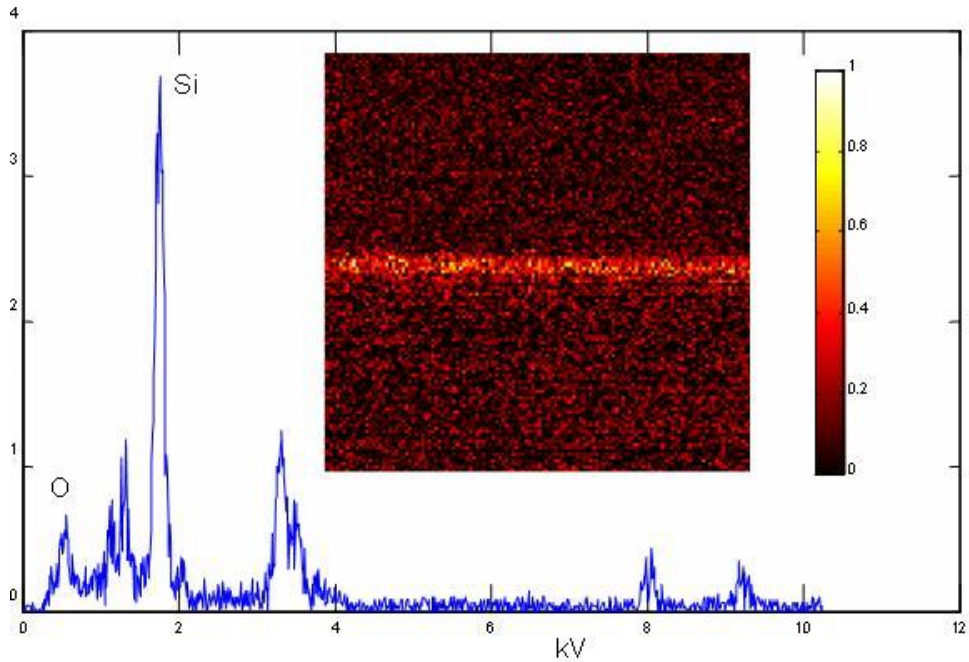


**Figure 33. X-ray spectrum from the interface layer for NREL 1-1006 Q4**

Table 14 summarizes the interface thickness for the three samples. Surprisingly the interface thickness does not decline for both treatments.

**Table 14. Treatments considered in the interface study.**

| Sample Number | Interface thickness [nm] |
|---|---|
| NREL 1-1006 Q1 | 15 |
| NREL 1-1006 Q2 | 18 |
| NREL 1-1006 Q4 | 12 |

## 4.3 XTEM analysis of 05-362a and 05-362b.

Two samples of a 3-step InPAs buffer grown on different miscuts from the (100) surface of InP were subjected to XTEM analysis. As with the previous study the samples were thinned to electron transparency with a FIB. The goal of this study was to evaluate if the dislocation structure and density were different for the two miscuts. Figure 34 shows an XTEM image for 05-362a, a 3-step buffer on a (100) substrate with a miscut of ±0.2° toward a (111) . The lower layers of the buffer, $InP_{0.84}As_{0.16}$ and $InP_{0.72}As_{0.28}$, contain several half loops with the ends of the loops propagating upward.

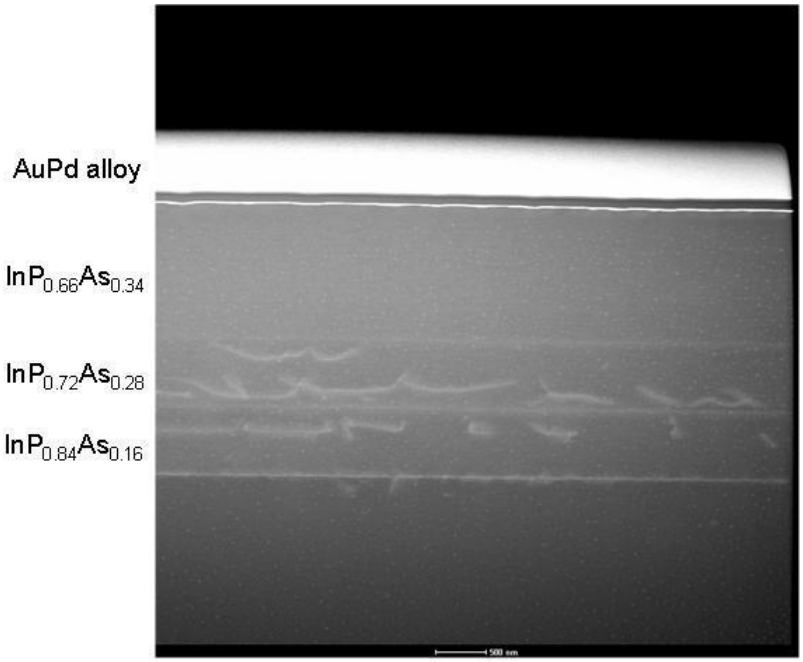


**Figure 34. XTEM image of 05-362a. The speckled texture is an artifact of the FIB process.**

None of the loops appear to propagate down from the subsequent layer, which has been proposed based on the critical composition difference theory for InGaAs grown on GaAs. The density of segments in the $InP_{0.84}As_{0.16}$ layer is 3.7 x $10^8$ $cm^{-2}$ and in the $InP_{0.72}As_{0.28}$layer the segment density is 4.8 x $10^8$ $cm^{-2}$. The top $InP_{0.66}As_{0.34}$ layer does not have any loops or other features. Figure 35 is a similar image for 05-362b, grown on a (100) substrate with a 2° miscut toward the (110) direction. The density of threading loops is similar in the $InP_{0.84}As_{0.16}$ and smaller for the $InP_{0.72}As_{0.28}$ layers for this sample than that grown on the ± 0.2° miscut substrate. The density of segments in the $InP_{0.84}As_{0.16}$ layer is 4.3 x $10^8$ $cm^{-2}$ and in the $InP_{0.72}As_{0.28}$layer the segment density is 5 x $10^7$ $cm^{-2}$. At the interface between $InP_{0.84}As_{0.16}$ and $InP_{0.72}As_{0.28}$ a few dislocation segments appear to be propagating down from the $InP_{0.72}As_{0.28}$ layer. As with 05-362a, no threading segments are observed in the $InP_{0.66}As_{0.34}$ layer. The lower dislocation

density in the $InP_{0.72}As_{0.28}$ for 05-362b is the significant difference between these two samples, suggesting a higher performing device might be grown on 2° miscut substrates.

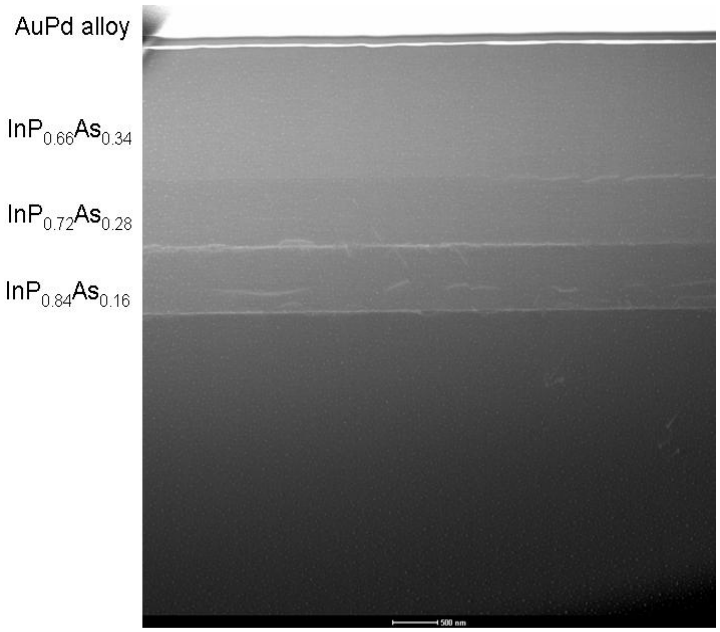


**Figure 35. XTEM image of 05-362b. The speckled texture is an artifact of the FIB process.**

## 4.4 Plan view TEM sample preparation

To baseline the defect sensitive etching studies a numeric correlation between the features observed and the threading dislocation density as measured by plan view (PV) TEM is needed. If the dislocation density in a layer is 1 x $10^6$ $cm^{-2}$, as has been proposed for InGaAs TPV cells grown on InPAs strain relaxed buffers, it would require a 1000 $\mu m^2$ area to find 10 dislocations to statistically verify the proposed density. Larger area samples are needed. Argon ion milling techniques might be able to produce a sample with this area. The time needed to thin the sample would be long, approaching days, and cryogenic conditions would need to be used to limit the evaporation of indium from the surface. Chemical jet etching with bromine-methanol solution is another possibility, but

the control of this technique is speculative. Chemical jet thinning also produces a dome shaped pit with only a limited area of the dome being transparent to high energy electrons. Since InP can be etched rapidly in an aqueous solution of 2:3 volume fraction HCl(32%):$H_3PO_4$(85%) this was investigated as a possible solution.[47] This leads to the process flow described in Figure 36 below. A small sample (5 mm x 5 mm) has the epilayer side coated with photoresist (AZ4330). The photoresist coated side is mounted to a glass slide with Crystalbond. The edges of sample are covered with a thick layer of photoresist, leaving an approximately 0.5 mm opening near the center of the sample.

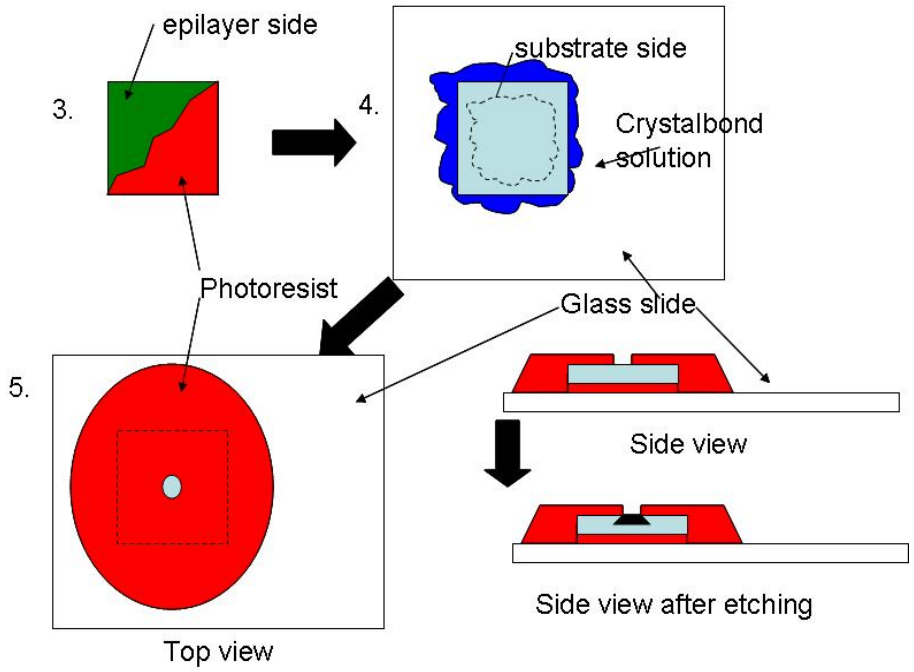


**Figure 36. Process flow diagram for chemical etching of a PV TEM foil.**

The coated sample is placed in a beaker with the etchant solution. The advertised selectivity of the etchant to InP compared to InPAs is not as strong as proposed. The InPAs is etched, but the rate is slower than that for InP. Etching for 3.5 hours produces a foil 35 µm thick. Interference contrast microscopy of the etched surface shown in Figure

37 shows mounds. The cross-sectional SEM image (Figure 37, right) gives the thickness of the foil.

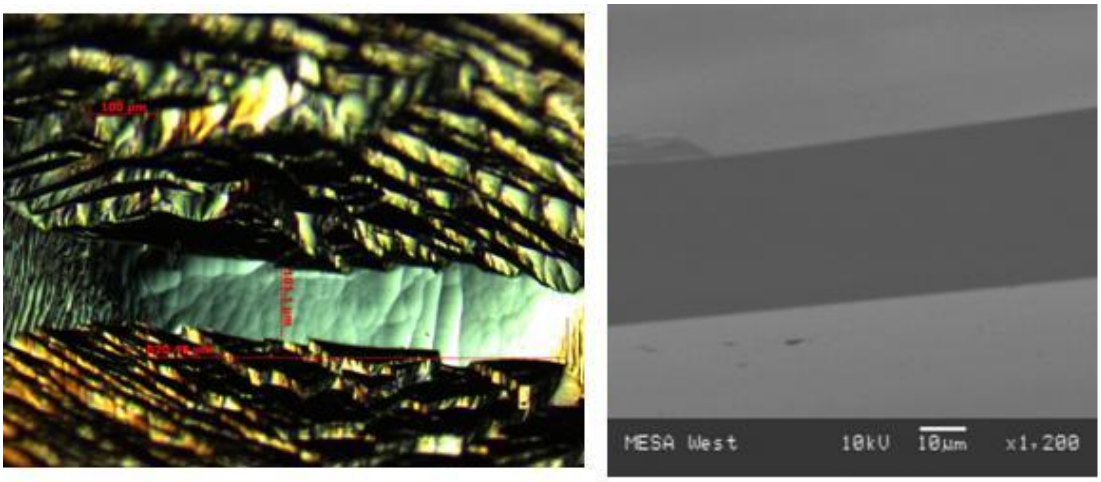


**Figure 37. a) The etched surface of bottom of the pit as viewed Nomarski contrast microscopy (left), b) SEM cross-section of foil after 3.5 hours of etching (right). Foil thickness is 35 µm.**

Extending the etch time to 4 hours produced a foil that is less than 2 µm thick. Figure 38 shows that the chemical etching has decorated the bottom of the foil. The foil is very fragile at this point and when removed from the Crystalbond it fractures easily. However, the foil that remains attached to the walls has enough area that the dislocation density could be determined with excellent statistics. The sample is still a factor of ten too thick to be transparent to high energy electrons used in PV TEM. This could be reduced by chemically etching the mounted membrane in dilute HCl.

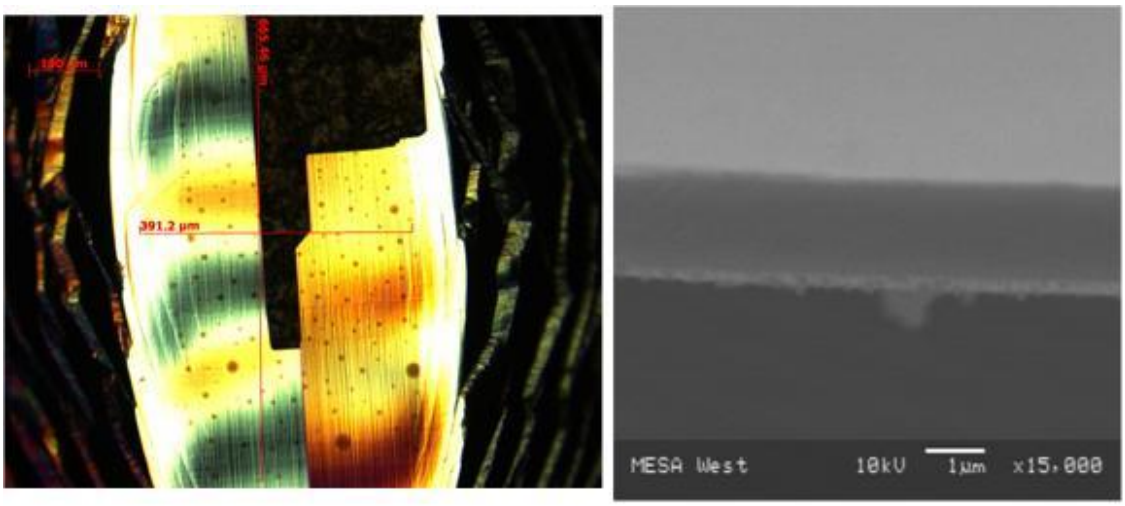


**Figure 38. The etched surface of bottom of the pit as viewed Nomarski contrast microscopy (left), SEM cross-section of foil after 4.0 hours of etching. Foil thickness is less than 2 µm.**

## 5 References

1. T. Marschner, M.R. Leys, H. Vonk, J.H. Wolter, Physica E, **2**, (1998), 873.
2. M.K. Hudait, Y. Lin, P.M. Sinha, J.R. Lindemuth, S.A. Ringel, J. Appl. Phys., (2006), accepted.
3. S-W. Ryu, H-D. Kim, S-K. Park, W.G. Jeong, B-D. Choe, Japan. J. Appl. Phys., **36**, (1997), L79.
4. T. Okada, R.V. Kruzelecky, G.C. Weatherly, D.A. Thompson, Appl. Phys. Lett., **63**, (1993), 3194.
5. J. Tersoff, Appl. Phys. Lett., **62**, (1993), 693.
6. D. González, D. Araájo, G. Aragón, R. Garcia, Appl. Phys. Lett., **72**, (1998), 1875.
7. I. Yonenaga, K. Sumino, Appl. Phys. Lett., **58**, (1991), 48.
8. G.K. Williamson, W.H. Hall, Acta Metallurgica, **1**, (1953), 22.
9. P. Gay, P.B. Hirsch, A. Kelly, Acta Metallurgica, **1**, (1953), 315.
10. C.G. Dunn, E.F. Koch, Acta Metallurgica, **5**, (1957), 548.
11 M.J. Hordon, B.L. Averbach, Acta Metallurgica, **9**, (1961), 237.
12. A.D. Kurtz, S.A. Kulin, B.L, Averbach, **101**, (1956), 1285
13. J.E. Ayers, J. Crystal Growth, **135**, (1994), 71.
14. S.R. Lee, A.M. West, A.A. Allerman, K.E. Waldrip, D.M. Follstaedt, P.P. Provencio, D.D. Koleske, C.R. Abernathy, Appl. Phys. Lett., **86**, (2005), 241904.
15 E. Koppensteiner, A. Schuh, G. Bauer, V. Holý, G.P. Watson, E.A. Fitzgerald, J. Phys. D: Appl. Phys., **28**, (1995), A114.
16. K. Akita, T. Kusunoki, S. Komiya, T. Kotani, J. Crystal Growth, **46**, (1979), 732.

17. S. Mahajan, A.K. Chin, J. Crystal Growth, **54**, (1981), 138.
18. T. Kotani, S. Komiya, S. Nakai, Y. Yamaoka, J. Electrochemical Soc., **127**, (1980), 2273.
19. A. Huber, N.T. Linh, J. Crystal Growth, **29,** (1975), 80.
20. D.J. Stirland, D.G. Hart, S. Clark, J.C. Regnault, C.R. Elliott, J. Crystal Growth, **61**, (1983), 645.
21. F.A. Thiel, R.L. Barns, J. Electrochemical Society, **126**, (1979), 1272.
22. R.C. Clarke, D.S. Robertson, A.W. Vere, J. Materials Science, **8**, (1973), 1349.
23. S.N.G. Chu, C.M. Jodlauk, A.A. Ballman, J. Electrochemical Society, **129**, (1982), 352.
24. M.S. Abrahams, C.J. Buiocchi, J. Appl. Phys., **36**, (1965), 2855.
25. Chen, J. Crystal Growth, **129**, (1993), 777.
26. Y. Hayakawa, S. Iida, T. Sakurai, H. Yanagida, M. Kikuzawa, T. Koyama, M. Kumagawa, J. Crystal Growth, **169**, (1996), 613
27. S. Komiya, K. Nakajima, J. Crystal Growth, **48**, (1980), 403.
28. P.D. Wright, E.A. Rezek, N. Holonyak, Jr., J. Crystal Growth, **41**, (1977), 254.
29. G.H. Olsen, M. Ettenberg, J. Appl. Phys., **45**, (1974), 5112.
30. J.L. Weyher, L.J. Giling, J. Appl. Phys., **58**, (1985), 219.
31. J.L. Weyher, R. Fornari, T. Görög, J.J. Kelly, B. Erné, J. Crystal Growth, **141**, (1994), 57.
32. W.R. Wagner, L.I. Greene, L.I. Koszi, J. Electrochemical Soc., **128**, (1981), 1091.
33. N. Susa, Y. Yamauchi, H. Ando, H. Kanbe, Jap. J. Appl. Phys., **19**, (1979), L17.
34. Y.G. Chai, R. Chow, J. Appl. Phys., **53**, (1982), 1229.
35. J. Weyher, J. Van De Ven, J. Crystal Growth, **63**, (1983), 285.
36. J. Weyher, W.J.P. Van Enckevort, J. Crystal Growth, **63**, (1983), 292.
37. J. Weyher, J. Van De Ven, J. Crystal Growth, **78**, (1986), 191.
38. J. Nishizawa, Y. Oyama, H. Tadano, K. Inokuchi, Y. Okuno, J. Crystal Growth, **47**, (1979), 434.
39. V. Gottschalch, R. Srnanek, G. Wagner, J. Materials Science Lett., **1**, (1982), 358.
40. J.L. Richards, A.J. Crocker, J. Appl. Phys., **30**, (1959), 611.
41. M.S. Abrahams, J. Appl. Phys., **35**, (1964), 3626.
42. I. Yonenaga, K. Sumino, Appl. Phys. Lett., **58**, (1991), 48
43. M. D'hondt, I. Moerman, P. Demeester, J. Crystal Growth, **170**, (1997), 616.
44. B. Tuck, J. Material Science, **10**, (1975), 321.
45. Y.G. Chai, R. Chow, J. Appl. Phys., **53**, (1982), 1229.
46. N. Susa, Y. Yamauchi, H. Ando, H. Kanbe, Japan. J. Appl. Phys., **19**, (1979), L17.
47. M. D'Hondt, I. Moerman, P. Demeester, J. Crystal Growth, **170**, (1997), 616.